L '(CO)/L-FIR RELATIONS WITH CO ROTATIONAL LADDERS OF GALAXIES ACROSS THE HERSCHEL SPIRE ARCHIVE

Item Type	Article
Authors	Kamenetzky, J. R.; Rangwala, N.; Glenn, J.; Maloney, P. R.; Conley, A.
Citation	L '(CO)/L-FIR RELATIONS WITH CO ROTATIONAL LADDERS OF GALAXIES ACROSS THE HERSCHEL SPIRE ARCHIVE 2016, 829 (2):93 The Astrophysical Journal
DOI	10.3847/0004-637X/829/2/93
Publisher	IOP PUBLISHING LTD
Journal	The Astrophysical Journal
Rights	© 2016. The American Astronomical Society. All rights reserved.
Download date	24/08/2022 13:21:51
Item License	http://rightsstatements.org/vocab/InC/1.0/
Version	Final published version
Link to Item	http://hdl.handle.net/10150/621957

CrossMark

L'_{CO}/L_{FIR} RELATIONS WITH CO ROTATIONAL LADDERS OF GALAXIES ACROSS THE *HERSCHEL* SPIRE ARCHIVE

J. KAMENETZKY[1,4], N. RANGWALA[2,5], J. GLENN[3], P. R. MALONEY[3], AND A. CONLEY[3]

[1] Steward Observatory, University of Arizona, 933 North Cherry Avenue, Tucson, AZ 85721, USA; jkamenetzky@as.arizona.edu
[2] NASA Ames Research Center Universities Space Research Association/Naval Air Station, Moffett Field, Mountain View, CA 94035, USA
[3] University of Colorado at Boulder, Center for Astrophysics and Space Astronomy, 389-UCB, Boulder, CO, USA

ABSTRACT

We present a catalog of all CO ($J = 4-3$ through $J = 13-12$), [C I], and [N II] lines available from extragalactic spectra from the *Herschel* SPIRE Fourier Transform Spectrometer (FTS) archive combined with observations of the low-J CO lines from the literature and from the Arizona Radio Observatory. This work examines the relationships between L_{FIR}, L'_{CO}, and $L_{CO}/L_{CO,1-0}$. We also present a new method for estimating probability distribution functions from marginal signal-to-noise ratio *Herschel* FTS spectra, which takes into account the instrumental "ringing" and the resulting highly correlated nature of the spectra. The slopes of $\log(L_{FIR})$ versus $\log(L'_{CO})$ are linear for all mid- to high-J CO lines and slightly sublinear if restricted to (ultra)luminous infrared galaxies ((U)LIRGs). The mid- to high-J CO luminosity relative to CO $J = 1-0$ increases with increasing L_{FIR}, indicating higher excitation of the molecular gas, although these ratios do not exceed ∼180. For a given bin in L_{FIR}, the luminosities relative to CO $J = 1-0$ remain relatively flat from $J = 6-5$ through $J = 13-12$, across three orders of magnitude of L_{FIR}. A single component theoretical photodissociation region (PDR) model cannot match these flat SLED shapes, although combinations of PDR models with mechanical heating added qualitatively match the shapes, indicating the need for further comprehensive modeling of the excitation processes of warm molecular gas in nearby galaxies.

Key words: galaxies: ISM – ISM: molecules – submillimeter: galaxies – submillimeter: ISM – surveys

Supporting material: machine-readable tables

1. INTRODUCTION

Within the multi-phase interstellar medium (ISM), molecular gas is the most intimately tied to star formation (SF), and therefore to the stellar lifecycle's dramatic effects on galaxy evolution. Although molecular hydrogen is the dominant component of such gas, pure H_2 rotational lines are difficult to detect and not particularly sensitive to the low temperatures of most molecular gases. Instead, ^{12}CO (henceforth CO) and its isotopologues are used to trace the mass, kinematics, and excitation of molecular gas. The ground-level CO $J = 1-0$ line is widely used to estimate the total molecular mass in the ISM, and ratios with higher lines provide information on the temperature and density of the emitting gas. Higher lines, however, are increasingly blocked by water absorption in Earth's atmosphere. It was not until the launch of the *Herschel Space Observatory* (Pilbratt et al. 2010) that the CO ladder up to $J = 13-12$ was generally available for the ISM within our Galaxy and in nearby galaxies.

Early SPIRE observations showed much brighter high-J CO emission than would be predicted by cool ($T_{kin} < 50$ K) molecular gas in giant molecular clouds, the type of gas responsible for the CO $J = 1-0$ and other low-J emission (e.g., Panuzzo et al. 2010; Rangwala et al. 2011; Kamenetzky et al. 2012; Spinoglio et al. 2012; Pereira-Santaella et al. 2013; Rigopoulou et al. 2013). A warmer, denser (higher pressure) component of molecular gas is responsible for the emission of mid-J ($J = 4-3$ to $J = 6-5$) to high-J ($J = 7-6$ and above) CO lines (and even warmer emission can be seen in the much higher-J lines visible with PACS, as in Hailey-Dunsheath et al. 2012).

UV heating from young O and B stars creates photodissociation regions (PDRs), which can reproduce the excitation and emission of the low-J lines. However, PDR models often cannot explain the bright emission seen in high-J lines, which may require mechanical excitation via shocks, turbulence, winds, and other dynamical processes within galaxies. In addition to illuminating the excitation mechanisms of the gas, CO emission is also studied in the context of the Kennicutt–Schmidt law (K–S law; Kennicutt 1998), which relates the gas surface density to the SF rate (SFR) surface density.

Now that *Herschel*'s mission is complete, work is underway to examine the full archival data set. Kamenetzky et al. (2014, henceforth K14) presented a two-component modeling procedure for a sample of galaxies observed with the *Herschel* SPIRE Fourier Transform Spectrometer (FTS). In the 17 galaxy systems studied in that paper, the warm molecular gas accounted for about 10% of the total molecular mass, but 90% of the CO luminosity. Here we expand this sample and compile a comprehensive, uniformly calibrated set of CO $J = 4-3$ to $J = 13-12$, [C I] (609 and 370 μm), and [N II] (205 μm) line fluxes for the galaxies observed by the *Herschel* SPIRE FTS, as well as a similarly matched set of CO $J = 1-0$ to $J = 3-2$ lines from the literature and the Arizona Radio Observatory (ARO). A future paper will include a full, two-component likelihood analysis of each galaxy's CO SLED, in order to derive cold and warm gas temperatures, densities, and masses, as in K14.

The observations and processing are described in Section 2. Section 3 presents the motivation for fitting the relationships between L'_{CO} and L_{FIR}, our results broken down by subsamples, and comparisons to the similar studies of Lu et al. (2014), Greve et al. (2014), and Liu et al. (2015). Discussion of trends and comparisons to theoretical models are in Section 4.

Table 1
Galaxies and Observations Utilized

Galaxy	R.A. J2000	Decl. J2000	$\log(L_{\rm FIR})$ $(L_\odot)$	D_L (Mpc)	$n_{\rm det}$	$n_{\rm ul}$	FTS ObsId	Phot ObsID
NGC 0023	$0^h09^m53^s36$	$+25^d55^m26^s4$	10.9	68	5	7	1342247622	1342234681
NGC 34	$0^h11^m06^s55$	$-12^d06^m26^s3$	11.2	85	12	0	1342199253	1342199383
MCG-02-01-051	$0^h18^m50^s86$	$-10^d22^m37^s5$	11.2	120	8	4	1342247617	1342234694
IC 10-B11-1	$0^h20^m27^s70$	$+59^d16^m59^s4$	7.5	1	8	5	1342246982	1342201446
IRAS 00188-0856	$0^h21^m26^s53$	$-08^d39^m27^s1$	12.2	591	4	5	1342246259	1342234693
ESO 350-IG038[a]	$0^h36^m52^s46$	$-33^d33^m17^s4$	10.8	87	1	8	1342246978	1342199386
NGC 205-copeak	$0^h40^m24^s10$	$+41^d41^m50^s4$	6.1	1	1	9	1342212315	1342188661
IRAS 00397-1312	$0^h42^m15^s53$	$-12^d56^m02^s8$	12.6	1285	0	7	1342246257	1342234696
NGC 0232a	$0^h42^m45^s82$	$-23^d33^m41^s7$	11.2	95	8	4	1342221707	1342234699
NGC 253	$0^h47^m33^s12$	$-25^d17^m17^s6$	10.3	3	12	1	1342210847	1342199387
I Zw 1[a]	$0^h53^m34^s94$	$+12^d41^m36^s2$	11.4	272	2	9	1342238246	1342238252
MCG+12-02-001	$0^h54^m03^s61$	$+73^d05^m11^s8$	11.2	72	11	2	1342213377	1342199365
NGC 0317B	$0^h57^m40^s37$	$+43^d47^m32^s4$	11.0	80	8	4	1342239358	1342238255
IRAS 01003-2238	$1^h02^m49^s90$	$-22^d21^m57^s3$	11.9	539	1	7	1342246256	1342234707
3C 31	$1^h07^m24^s96$	$+32^d24^m45^s2$	⋯	75	3	5	1342239344	1342236245
IC 1623	$1^h07^m47^s00$	$-17^d30^m25^s0$	11.4	86	11	1	1342212314	1342199388
MCG-03-04-014[a]	$1^h10^m08^s92$	$-16^d51^m11^s1$	11.4	152	6	6	1342213442	1342234709
ESO 244-G012[a]	$1^h18^m08^s26$	$-44^d27^m43^s0$	11.1	95	5	6	1342221708	1342234726
CGCG 436-030[a]	$1^h20^m02^s58$	$+14^d21^m42^s5$	11.5	138	9	3	1342213443	1342237499
ESO 353-G020	$1^h34^m51^s29$	$-36^d08^m15^s0$	10.8	66	7	5	1342247615	1342234721
IRAS F01417+1651	$1^h44^m30^s52$	$+17^d06^m08^s9$	⋯	120	7	5	1342239343	1342237555
NGC 0695	$1^h51^m14^s28$	$+22^d34^m55^s2$	11.4	143	6	5	1342224767	1342238266
Mrk 1014[a]	$1^h59^m50^s21$	$+00^d23^m40^s6$	12.3	763	1	7	1342238707	1342237540
NGC 0828	$2^h10^m09^s50$	$+39^d11^m24^s7$	11.1	80	4	7	1342239357	1342239822
NGC 0877a	$2^h18^m00^s12$	$+14^d32^m34^s2$	⋯	57	5	7	1342239342	1342238267
NGC 891-1	$2^h22^m33^s41$	$+42^d20^m56^s9$	10.2	10	7	5	1342213376	1342189430
UGC 01845	$2^h24^m07^s89$	$+47^d58^m11^s3$	10.9	70	5	7	1342240022	1342239799
NGC 0958	$2^h30^m42^s80$	$-02^d56^m23^s7$	10.9	82	3	7	1342239339	1342238277
0235+164	$2^h38^m38^s93$	$+16^d36^m59^s3$	⋯	4278	0	1	1342249452	1342224149
NGC 1068	$2^h42^m40^s71$	$-00^d00^m47^s8$	10.9	16	13	0	1342213445	1342189425
NGC 1056	$2^h42^m48^s30$	$+28^d34^m27^s1$	9.7	24	5	8	1342204024	1342226630
UGC 02238	$2^h46^m17^s50$	$+13^d05^m44^s9$	11.1	93	5	5	1342239340	1342238270
NGC 1097	$2^h46^m19^s00$	$-30^d16^m30^s0$	10.4	16	8	5	1342239337	1342188586
UGC 02369	$2^h54^m01^s81$	$+14^d58^m14^s3$	11.4	142	8	3	1342239341	1342239831
NGC 1222	$3^h08^m56^s74$	$-02^d57^m18^s5$	10.4	35	8	5	1342239354	1342239262
UGC 02608	$3^h15^m01^s24$	$+42^d02^m09^s2$	11.1	104	4	5	1342239356	1342239819
NGC 1266	$3^h16^m00^s70$	$-02^d25^m38^s0$	10.2	31	13	0	1342239353	1342189424
IRAS 03158+4227[a]	$3^h19^m12^s40$	$+42^d38^m28^s0$	12.4	623	4	4	1342224764	1342226656
3C 84	$3^h19^m48^s16$	$+41^d30^m42^s1$	10.8	78	11	2	1342249054	1342203614
NGC 1365-SW	$3^h33^m35^s90$	$-36^d08^m35^s0$	10.8	21	10	2	1342204021	1342201432
NGC 1365-NE	$3^h33^m36^s60$	$-36^d08^m20^s0$	10.8	21	10	3	1342204020	1342201432
NGC 1377	$3^h36^m39^s10$	$-20^d54^m08^s0$	9.7	24	12	1	1342239352	1342189505
NGC 1482	$3^h54^m38^s90$	$-20^d30^m09^s0$	10.5	25	12	1	1342248233	1342189504
IRAS 03521+0028[a]	$3^h54^m42^s19$	$+00^d37^m02^s0$	12.3	709	2	7	1342238704	1342239850
UGC 02982	$4^h12^m22^s53$	$+05^d32^m50^s4$	10.9	77	3	7	1342240021	1342239938
ESO 420-G013[a]	$4^h13^m49^s65$	$-32^d00^m24^s1$	10.7	49	8	5	1342242590	1342227719
NGC 1572[a]	$4^h22^m42^s81$	$-40^d36^m03^s2$	11.0	86	6	5	1342242588	1342227720
IRAS04271+3849	$4^h30^m33^s10$	$+38^d55^m48^s4$	10.9	86	6	4	1342227786	1342229106
NGC 1614	$4^h33^m59^s85$	$-08^d34^m44^s0$	11.3	68	12	1	1342192831	1342203628
UGC 03094	$4^h35^m33^s75$	$+19^d10^m17^s5$	11.1	108	4	6	1342227522	1342239944
MCG-05-12-006[a]	$4^h52^m04^s96$	$-32^d59^m25^s9$	10.9	78	6	4	1342242589	1342229237
IRAS F05189-2524[a]	$5^h21^m01^s47$	$-25^d21^m45^s4$	11.8	185	10	2	1342192833	1342203632
IRAS05223+1908	$5^h25^m16^s65$	$+19^d10^m48^s5$	⋯	130	2	0	1342228738	1342229652
MCG+08-11-002	$5^h40^m43^s65$	$+49^d41^m41^s8$	11.2	86	9	3	1342230414	1342229112
NGC 1961	$5^h42^m04^s37$	$+69^d22^m41^s9$	10.7	61	9	4	1342228708	1342227742
UGC 03351	$5^h45^m48^s00$	$+58^d42^m03^s7$	11.1	67	6	6	1342230415	1342229115
IRAS05442+1732	$5^h47^m11^s15$	$+17^d33^m47^s2$	11.0	81	5	5	1342230413	1342229653
IRAS 06035-7102	$6^h02^m54^s01$	$-71^d03^m10^s2$	12.0	353	10	2	1342230420	
UGC 03410a	$6^h14^m29^s64$	$+80^d26^m59^s4$	10.8	61	3	8	1342231072	1342229131
NGC 2146-NW	$6^h18^m36^s70$	$+78^d21^m32^s0$	10.8	17	12	0	1342219554	1342191186
NGC 2146-nuc	$6^h18^m38^s60$	$+78^d21^m24^s0$	10.8	17	11	2	1342204025	1342191186
NGC 2146-SE	$6^h18^m40^s50$	$+78^d21^m16^s0$	10.8	17	11	2	1342219555	1342191186
IRAS 06206-6315[a]	$6^h21^m01^s21$	$-63^d17^m23^s5$	12.0	411	4	5	1342231038	1342226638

Table 1
(Continued)

Galaxy	R.A. J2000	Decl. J2000	$\log(L_{\mathrm{FIR}})$ $(L_\odot)$	D_L (Mpc)	n_{det}	n_{ul}	FTS ObsId	Phot ObsID
ESO 255-IG007[a]	$6^{\mathrm{h}}27^{\mathrm{m}}21^{\mathrm{s}}63$	$-47^{\mathrm{d}}10^{\mathrm{m}}36^{\mathrm{s}}3$	$\cdots$	166	7	4	1342231084	1342226643
UGC 03608	$6^{\mathrm{h}}57^{\mathrm{m}}34^{\mathrm{s}}42$	$+46^{\mathrm{d}}24^{\mathrm{m}}10^{\mathrm{s}}7$	11.1	97	6	6	1342228744	1342229649
NGC 2342b	$7^{\mathrm{h}}09^{\mathrm{m}}12^{\mathrm{s}}09$	$+20^{\mathrm{d}}36^{\mathrm{m}}13^{\mathrm{s}}1$	10.8	77	5	6	1342228730	1342230778
NGC 2342a	$7^{\mathrm{h}}09^{\mathrm{m}}18^{\mathrm{s}}05$	$+20^{\mathrm{d}}38^{\mathrm{m}}10^{\mathrm{s}}0$	10.8	77	5	5	1342228729	1342230778
NGC 2369	$7^{\mathrm{h}}16^{\mathrm{m}}37^{\mathrm{s}}60$	$-62^{\mathrm{d}}20^{\mathrm{m}}35^{\mathrm{s}}9$	10.8	43	10	3	1342231083	1342229670
NGC 2388a	$7^{\mathrm{h}}28^{\mathrm{m}}53^{\mathrm{s}}43$	$+33^{\mathrm{d}}49^{\mathrm{m}}08^{\mathrm{s}}4$	11.0	62	7	6	1342231071	1342229477
MCG+02-20-003	$7^{\mathrm{h}}35^{\mathrm{m}}43^{\mathrm{s}}44$	$+11^{\mathrm{d}}42^{\mathrm{m}}34^{\mathrm{s}}8$	10.8	72	7	6	1342228728	1342229463
IRAS 07598+6508[a]	$8^{\mathrm{h}}04^{\mathrm{m}}30^{\mathrm{s}}45$	$+64^{\mathrm{d}}59^{\mathrm{m}}52^{\mathrm{s}}2$	12.1	693	0	10	1342253659	1342229642
B2 0827+24	$8^{\mathrm{h}}30^{\mathrm{m}}52^{\mathrm{s}}09$	$+24^{\mathrm{d}}10^{\mathrm{m}}59^{\mathrm{s}}8$	$\cdots$	5818	0	1	1342253660	1342230773
IRAS 08311-2459[a]	$8^{\mathrm{h}}33^{\mathrm{m}}20^{\mathrm{s}}60$	$-25^{\mathrm{d}}09^{\mathrm{m}}33^{\mathrm{s}}7$	12.2	451	9	1	1342230421	1342230796
He2-10	$8^{\mathrm{h}}36^{\mathrm{m}}15^{\mathrm{s}}18$	$-26^{\mathrm{d}}24^{\mathrm{m}}33^{\mathrm{s}}9$	9.6	10	9	3	1342245083	1342196888
IRAS08355-4944	$8^{\mathrm{h}}37^{\mathrm{m}}01^{\mathrm{s}}86$	$-49^{\mathrm{d}}54^{\mathrm{m}}30^{\mathrm{s}}0$	$\cdots$	110	7	5	1342231975	1342226978
NGC 2623	$8^{\mathrm{h}}38^{\mathrm{m}}24^{\mathrm{s}}08$	$+25^{\mathrm{d}}45^{\mathrm{m}}16^{\mathrm{s}}6$	11.4	81	12	0	1342219553	1342206174
IRAS 08572+3915	$9^{\mathrm{h}}00^{\mathrm{m}}25^{\mathrm{s}}39$	$+39^{\mathrm{d}}03^{\mathrm{m}}54^{\mathrm{s}}4$	11.8	261	2	8	1342231978	1342230749
IRAS09022-3615	$9^{\mathrm{h}}04^{\mathrm{m}}12^{\mathrm{s}}72$	$-36^{\mathrm{d}}27^{\mathrm{m}}01^{\mathrm{s}}3$	12.0	262	11	1	1342231063	1342230799
NGC 2764	$9^{\mathrm{h}}08^{\mathrm{m}}17^{\mathrm{s}}47$	$+21^{\mathrm{d}}26^{\mathrm{m}}36^{\mathrm{s}}0$	10.0	40	5	7	1342231057	1342245567
NGC 2798	$9^{\mathrm{h}}17^{\mathrm{m}}22^{\mathrm{s}}90$	$+41^{\mathrm{d}}59^{\mathrm{m}}59^{\mathrm{s}}0$	10.4	28	12	1	1342252892	1342197287
UGC 05101	$9^{\mathrm{h}}35^{\mathrm{m}}51^{\mathrm{s}}65$	$+61^{\mathrm{d}}21^{\mathrm{m}}11^{\mathrm{s}}3$	11.8	176	9	3	1342209278	1342204962
NGC 2976_00	$9^{\mathrm{h}}47^{\mathrm{m}}07^{\mathrm{s}}84$	$+67^{\mathrm{d}}55^{\mathrm{m}}52^{\mathrm{s}}3$	$\cdots$	4	1	10	1342228706	1342192106
M81	$9^{\mathrm{h}}55^{\mathrm{m}}33^{\mathrm{s}}17$	$+69^{\mathrm{d}}03^{\mathrm{m}}55^{\mathrm{s}}0$	9.2	4	3	9	1342209851	1342185538
M82	$9^{\mathrm{h}}55^{\mathrm{m}}52^{\mathrm{s}}22$	$+69^{\mathrm{d}}40^{\mathrm{m}}46^{\mathrm{s}}9$	10.4	4	13	0	1342208389	1342185537
NGC 3077	$10^{\mathrm{h}}03^{\mathrm{m}}19^{\mathrm{s}}10$	$+68^{\mathrm{d}}44^{\mathrm{m}}02^{\mathrm{s}}0$	7.7	1	1	9	1342228745	1342193015
NGC 3110a	$10^{\mathrm{h}}04^{\mathrm{m}}02^{\mathrm{s}}09$	$-06^{\mathrm{d}}28^{\mathrm{m}}28^{\mathrm{s}}6$	11.0	73	4	6	1342231971	1342234843
3C 236	$10^{\mathrm{h}}06^{\mathrm{m}}01^{\mathrm{s}}74$	$+34^{\mathrm{d}}54^{\mathrm{m}}10^{\mathrm{s}}4$	$\cdots$	451	0	6	1342246988	1342246613
NGC 3221	$10^{\mathrm{h}}22^{\mathrm{m}}20^{\mathrm{s}}20$	$+21^{\mathrm{d}}34^{\mathrm{m}}22^{\mathrm{s}}4$	10.7	61	2	8	1342221714	1342246610
NGC 3227[a]	$10^{\mathrm{h}}23^{\mathrm{m}}30^{\mathrm{s}}58$	$+19^{\mathrm{d}}51^{\mathrm{m}}54^{\mathrm{s}}2$	9.7	18	12	1	1342209281	1342197318
NGC 3256	$10^{\mathrm{h}}27^{\mathrm{m}}51^{\mathrm{s}}27$	$-43^{\mathrm{d}}54^{\mathrm{m}}13^{\mathrm{s}}8$	11.3	38	13	0	1342201201	1342200126
IRAS 10378+1109	$10^{\mathrm{h}}40^{\mathrm{m}}29^{\mathrm{s}}17$	$+10^{\mathrm{d}}53^{\mathrm{m}}18^{\mathrm{s}}3$	12.1	631	2	8	1342247118	1342234867
ESO 264-G036	$10^{\mathrm{h}}43^{\mathrm{m}}07^{\mathrm{s}}68$	$-46^{\mathrm{d}}12^{\mathrm{m}}44^{\mathrm{s}}9$	10.9	89	6	4	1342249044	1342236204
NGC 3351	$10^{\mathrm{h}}43^{\mathrm{m}}57^{\mathrm{s}}70$	$+11^{\mathrm{d}}42^{\mathrm{m}}14^{\mathrm{s}}0$	9.7	13	9	4	1342247117	1342198885
ESO 264-G057	$10^{\mathrm{h}}59^{\mathrm{m}}01^{\mathrm{s}}82$	$-43^{\mathrm{d}}26^{\mathrm{m}}25^{\mathrm{s}}9$	10.7	72	6	5	1342249043	1342236203
IRAS F10565+2448	$10^{\mathrm{h}}59^{\mathrm{m}}18^{\mathrm{s}}17$	$+24^{\mathrm{d}}32^{\mathrm{m}}34^{\mathrm{s}}4$	11.8	192	10	2	1342247096	1342234869
NGC 3521	$11^{\mathrm{h}}05^{\mathrm{m}}48^{\mathrm{s}}60$	$-00^{\mathrm{d}}02^{\mathrm{m}}09^{\mathrm{s}}0$	10.1	12	6	3	1342247743	1342198568
IRAS 11095-0238	$11^{\mathrm{h}}12^{\mathrm{m}}03^{\mathrm{s}}38$	$-02^{\mathrm{d}}54^{\mathrm{m}}23^{\mathrm{s}}8$	12.0	482	4	5	1342247760	1342234863
NGC 3627	$11^{\mathrm{h}}20^{\mathrm{m}}15^{\mathrm{s}}00$	$+12^{\mathrm{d}}59^{\mathrm{m}}30^{\mathrm{s}}0$	10.2	12	13	0	1342247604	1342198883
NGC 3665	$11^{\mathrm{h}}24^{\mathrm{m}}43^{\mathrm{s}}67$	$+38^{\mathrm{d}}45^{\mathrm{m}}46^{\mathrm{s}}0$	9.7	32	2	7	1342247121	1342222667
Arp 299-B	$11^{\mathrm{h}}28^{\mathrm{m}}31^{\mathrm{s}}00$	$+58^{\mathrm{d}}33^{\mathrm{m}}41^{\mathrm{s}}0$	11.6	49	13	0	1342199249	1342199345
Arp 299-C	$11^{\mathrm{h}}28^{\mathrm{m}}31^{\mathrm{s}}00$	$+58^{\mathrm{d}}33^{\mathrm{m}}50^{\mathrm{s}}0$	11.6	49	13	0	1342199250	1342199345
Arp 299-A	$11^{\mathrm{h}}28^{\mathrm{m}}33^{\mathrm{s}}63$	$+58^{\mathrm{d}}33^{\mathrm{m}}47^{\mathrm{s}}0$	11.6	49	13	0	1342199248	1342199345
PG 1126-041	$11^{\mathrm{h}}29^{\mathrm{m}}16^{\mathrm{s}}66$	$-04^{\mathrm{d}}24^{\mathrm{m}}07^{\mathrm{s}}6$	$\cdots$	266	1	9	1342247119	1342247271
ESO 320-G030	$11^{\mathrm{h}}53^{\mathrm{m}}11^{\mathrm{s}}72$	$-39^{\mathrm{d}}07^{\mathrm{m}}48^{\mathrm{s}}9$	11.0	45	12	1	1342210861	1342200129
NGC 3982[a]	$11^{\mathrm{h}}56^{\mathrm{m}}28^{\mathrm{s}}13$	$+55^{\mathrm{d}}07^{\mathrm{m}}30^{\mathrm{s}}9$	9.8	21	5	5	1342209277	1342186862
NGC 4038	$12^{\mathrm{h}}01^{\mathrm{m}}53^{\mathrm{s}}00$	$-18^{\mathrm{d}}52^{\mathrm{m}}01^{\mathrm{s}}0$	$\cdots$	23	6	5	1342210860	1342188686
NGC 4038overlap	$12^{\mathrm{h}}01^{\mathrm{m}}54^{\mathrm{s}}90$	$-18^{\mathrm{d}}52^{\mathrm{m}}46^{\mathrm{s}}0$	$\cdots$	23	8	4	1342210859	1342188686
NGC 4051[a]	$12^{\mathrm{h}}03^{\mathrm{m}}09^{\mathrm{s}}61$	$+44^{\mathrm{d}}31^{\mathrm{m}}52^{\mathrm{s}}8$	9.5	14	9	4	1342209276	1342210502
IRAS 12071-0444	$12^{\mathrm{h}}09^{\mathrm{m}}45^{\mathrm{s}}12$	$-05^{\mathrm{d}}01^{\mathrm{m}}13^{\mathrm{s}}9$	12.1	591	2	8	1342248239	1342234858
NGC 4151[a]	$12^{\mathrm{h}}10^{\mathrm{m}}32^{\mathrm{s}}58$	$+39^{\mathrm{d}}24^{\mathrm{m}}20^{\mathrm{s}}6$	$\cdots$	18	5	7	1342209852	1342188588
NGC 4194	$12^{\mathrm{h}}14^{\mathrm{m}}09^{\mathrm{s}}63$	$+54^{\mathrm{d}}31^{\mathrm{m}}36^{\mathrm{s}}1$	10.7	39	10	3	1342231069	1342230869
IRAS12116-5615	$12^{\mathrm{h}}14^{\mathrm{m}}22^{\mathrm{s}}17$	$-56^{\mathrm{d}}32^{\mathrm{m}}32^{\mathrm{s}}8$	11.3	115	10	2	1342249462	1342226974
NGC 4254	$12^{\mathrm{h}}18^{\mathrm{m}}49^{\mathrm{s}}60$	$+14^{\mathrm{d}}24^{\mathrm{m}}59^{\mathrm{s}}0$	10.8	36	5	4	1342236997	1342187173
NGC 4321	$12^{\mathrm{h}}22^{\mathrm{m}}54^{\mathrm{s}}90$	$+15^{\mathrm{d}}49^{\mathrm{m}}21^{\mathrm{s}}0$	10.4	25	8	4	1342247572	1342187322
NGC 4388	$12^{\mathrm{h}}25^{\mathrm{m}}46^{\mathrm{s}}75$	$+12^{\mathrm{d}}39^{\mathrm{m}}43^{\mathrm{s}}5$	10.4	38	10	3	1342210849	1342248482
NGC 4459	$12^{\mathrm{h}}29^{\mathrm{m}}00^{\mathrm{s}}03$	$+13^{\mathrm{d}}58^{\mathrm{m}}42^{\mathrm{s}}8$	9.1	19	3	7	1342248411	1342200118
NGC 4526	$12^{\mathrm{h}}34^{\mathrm{m}}03^{\mathrm{s}}03$	$+07^{\mathrm{d}}41^{\mathrm{m}}56^{\mathrm{s}}9$	9.1	10	6	6	1342224762	1342234889
NGC 4536	$12^{\mathrm{h}}34^{\mathrm{m}}27^{\mathrm{s}}00$	$+02^{\mathrm{d}}11^{\mathrm{m}}17^{\mathrm{s}}0$	10.5	27	9	4	1342237025	1342189455
NGC 4569	$12^{\mathrm{h}}36^{\mathrm{m}}49^{\mathrm{s}}80$	$+13^{\mathrm{d}}09^{\mathrm{m}}46^{\mathrm{s}}0$	7.5	1	10	3	1342248251	1342188777
TOL 1238-364	$12^{\mathrm{h}}40^{\mathrm{m}}52^{\mathrm{s}}85$	$-36^{\mathrm{d}}45^{\mathrm{m}}21^{\mathrm{s}}1$	10.4	46	7	6	1342213381	1342202200
NGC 4631	$12^{\mathrm{h}}42^{\mathrm{m}}08^{\mathrm{s}}00$	$+32^{\mathrm{d}}32^{\mathrm{m}}29^{\mathrm{s}}0$	10.4	12	7	3	1342247573	1342188756
NGC 4710	$12^{\mathrm{h}}49^{\mathrm{m}}38^{\mathrm{s}}96$	$+15^{\mathrm{d}}09^{\mathrm{m}}55^{\mathrm{s}}8$	9.6	18	5	8	1342247120	1342188766
NGC 4736	$12^{\mathrm{h}}50^{\mathrm{m}}53^{\mathrm{s}}00$	$+41^{\mathrm{d}}07^{\mathrm{m}}14^{\mathrm{s}}0$	9.9	8	7	4	1342245851	1342188754
Mrk 231	$12^{\mathrm{h}}56^{\mathrm{m}}14^{\mathrm{s}}23$	$+56^{\mathrm{d}}52^{\mathrm{m}}25^{\mathrm{s}}2$	12.2	188	11	1	1342210493	1342201218
NGC 4826	$12^{\mathrm{h}}56^{\mathrm{m}}43^{\mathrm{s}}70$	$+21^{\mathrm{d}}40^{\mathrm{m}}58^{\mathrm{s}}0$	9.7	9	8	3	1342246992	1342188764
MCG-02-33-098	$13^{\mathrm{h}}02^{\mathrm{m}}19^{\mathrm{s}}80$	$-15^{\mathrm{d}}46^{\mathrm{m}}03^{\mathrm{s}}5$	10.7	69	4	7	1342247567	1342234810

Table 1
(Continued)

Galaxy	R.A. J2000	Decl. J2000	$\log(L_{\mathrm{FIR}})$ ($L_\odot$)	D_L (Mpc)	n_{det}	n_{ul}	FTS ObsId	Phot ObsID
ESO 507-G070	13^{h}02^{m}52^{s}34	−23^{d}55^{m}17^{s}8	11.2	91	11	1	1342248421	1342234813
NGC 5010	13^{h}12^{m}26^{s}39	−15^{d}47^{m}51^{s}7	10.6	43	6	5	1342236996	1342234809
IRAS13120-5453	13^{h}15^{m}06^{s}35	−55^{d}09^{m}22^{s}7	12.0	132	12	0	1342212342	1342226970
NGC 5055	13^{h}15^{m}49^{s}30	+42^{d}01^{m}45^{s}0	10.1	11	5	6	1342237026	1342188753
Arp 193	13^{h}20^{m}35^{s}34	+34^{d}08^{m}22^{s}2	11.4	105	12	0	1342209853	1342198191
NGC 5104	13^{h}21^{m}23^{s}09	+00^{d}20^{m}33^{s}3	10.9	82	5	6	1342247566	1342236168
MCG-03-34-064[a]	13^{h}22^{m}24^{s}42	−16^{d}43^{m}42^{s}7	⋯	74	8	3	1342249041	1342236178
Cen A	13^{h}25^{m}27^{s}61	−43^{d}01^{m}08^{s}8	9.7	4	8	5	1342204037	1342188663
NGC 5135	13^{h}25^{m}44^{s}06	−29^{d}50^{m}01^{s}2	11.0	58	12	0	1342212344	1342202248
ESO 173-G015	13^{h}27^{m}23^{s}78	−57^{d}29^{m}22^{s}2	11.2	39	13	0	1342202268	1342203562
NGC 5194	13^{h}29^{m}52^{s}71	+47^{d}11^{m}42^{s}6	10.4	11	7	6	1342201202	1342188589
IC 4280	13^{h}32^{m}53^{s}35	−24^{d}12^{m}25^{s}4	10.7	70	6	4	1342249042	1342236191
M83	13^{h}37^{m}00^{s}92	−29^{d}51^{m}56^{s}7	10.4	7	10	2	1342212345	1342188664
Mrk 273	13^{h}44^{m}42^{s}11	+55^{d}53^{m}12^{s}7	12.0	168	11	1	1342209850	1342201217
4C 12.50[a]	13^{h}47^{m}33^{s}36	+12^{d}17^{m}24^{s}2	12.0	561	1	9	1342237024	1342234792
UGC 08739	13^{h}49^{m}14^{s}28	+35^{d}15^{m}19^{s}8	10.8	76	6	6	1342247123	1342236144
ESO 221-IG010	13^{h}50^{m}56^{s}87	−49^{d}03^{m}18^{s}5	10.5	39	5	6	1342249461	1342238293
Mrk 463[a]	13^{h}56^{m}02^{s}87	+18^{d}22^{m}19^{s}5	11.2	226	4	7	1342249047	1342236151
M101_02	14^{h}03^{m}41^{s}36	+54^{d}19^{m}04^{s}9	10.1	8	2	10	1342230417	1342188750
OQ 208[a]	14^{h}07^{m}00^{s}39	+28^{d}27^{m}14^{s}7	⋯	348	3	6	1342247769	1342234785
NGC 5653	14^{h}30^{m}09^{s}88	+31^{d}12^{m}56^{s}3	10.8	55	5	8	1342247565	1342236146
IRAS 14348-1447	14^{h}37^{m}38^{s}26	−15^{d}00^{m}24^{s}6	12.1	371	8	3	1342249457	1342238301
NGC 5713	14^{h}40^{m}11^{s}50	−00^{d}17^{m}20^{s}0	10.5	29	8	5	1342248250	1342189520
IRAS 14378-3651	14^{h}40^{m}59^{s}01	−37^{d}04^{m}32^{s}0	11.9	303	10	1	1342227456	1342238295
Mrk 478[a]	14^{h}42^{m}07^{s}46	+35^{d}26^{m}22^{s}9	11.1	358	0	9	1342238710	1342238333
NGC 5734a	14^{h}45^{m}08^{s}98	−20^{d}52^{m}13^{s}4	10.7	59	3	10	1342248417	1342227731
3C 305[a]	14^{h}49^{m}21^{s}80	+63^{d}16^{m}15^{s}3	⋯	187	1	4	1342236998	1342234915
VV 340a[a]	14^{h}57^{m}00^{s}66	+24^{d}37^{m}05^{s}1	⋯	145	6	5	1342238241	1342234779
IC 4518ABa	14^{h}57^{m}41^{s}15	−43^{d}07^{m}56^{s}2	⋯	68	7	4	1342250514	1342239895
NGC 5866[a]	15^{h}06^{m}29^{s}50	+55^{d}45^{m}47^{s}6	9.4	14	7	4	1342238708	1342188749
CGCG 049-057	15^{h}13^{m}13^{s}09	+07^{d}13^{m}31^{s}8	11.1	59	11	2	1342212346	1342203077
3C 315	15^{h}13^{m}40^{s}08	+26^{d}07^{m}31^{s}2	⋯	498	0	4	1342239350	1342234777
VV 705[a]	15^{h}18^{m}06^{s}13	+42^{d}44^{m}44^{s}5	⋯	181	10	2	1342238712	1342229532
ESO 099-G004	15^{h}24^{m}57^{s}99	−63^{d}07^{m}30^{s}2	11.4	125	10	2	1342230419	1342229209
IRAS 15250+3609	15^{h}26^{m}59^{s}40	+35^{d}58^{m}37^{s}5	11.8	248	2	9	1342238711	1342234775
NGC 5936	15^{h}30^{m}00^{s}80	+12^{d}59^{m}21^{s}7	10.8	61	6	5	1342249046	1342238324
Arp 220	15^{h}34^{m}57^{s}12	+23^{d}30^{m}11^{s}5	12.0	81	11	2	1342190674	1342188687
NGC 5990	15^{h}46^{m}16^{s}40	+02^{d}24^{m}54^{s}7	10.7	57	6	7	1342240016	1342238312
IRAS 15462-0450	15^{h}48^{m}56^{s}81	−04^{d}59^{m}33^{s}6	12.0	456	3	7	1342249045	1342238307
3C 326	15^{h}52^{m}09^{s}07	+20^{d}05^{m}48^{s}4	⋯	407	0	7	1342250516	1342238327
PKS 1549-79	15^{h}56^{m}58^{s}87	−79^{d}14^{m}04^{s}3	⋯	690	0	8	1342253671	1342239890
NGC 6052	16^{h}05^{m}12^{s}94	+20^{d}32^{m}36^{s}9	10.8	71	6	6	1342212347	1342229560
IRAS 16090-0139	16^{h}11^{m}40^{s}48	−01^{d}47^{m}05^{s}6	12.3	618	6	4	1342238699	1342229565
PG 1613+658	16^{h}13^{m}57^{s}18	+65^{d}43^{m}09^{s}6	11.5	600	0	8	1342242593	1342238336
CGCG 052-037	16^{h}30^{m}56^{s}60	+04^{d}04^{m}58^{s}3	11.1	109	8	2	1342251284	1342229572
NGC 6156	16^{h}34^{m}52^{s}50	−60^{d}37^{m}07^{s}7	10.8	45	8	4	1342231041	1342229213
ESO 069-IG006	16^{h}38^{m}11^{s}84	−68^{d}26^{m}08^{s}5	11.7	203	7	4	1342231040	1342230810
IRAS F16399-0937	16^{h}42^{m}40^{s}10	−09^{d}43^{m}13^{s}6	11.3	118	8	4	1342251334	1342229188
NGC 6240	16^{h}52^{m}58^{s}89	+02^{d}24^{m}03^{s}4	11.6	108	13	0	1342214831	1342203586
IRAS F16516-0948	16^{h}54^{m}23^{s}81	−09^{d}53^{m}21^{s}4	11.0	100	6	5	1342251335	1342229189
NGC 6286b	16^{h}58^{m}23^{s}99	+58^{d}57^{m}20^{s}3	11.1	85	2	8	1342231068	1342229148
NGC 6286a	16^{h}58^{m}31^{s}56	+58^{d}56^{m}12^{s}2	11.1	85	7	3	1342221715	1342229148
IRAS F17138-1017	17^{h}16^{m}35^{s}82	−10^{d}20^{m}41^{s}5	11.1	76	8	3	1342230418	1342229190
IRAS F17207-0014	17^{h}23^{m}21^{s}96	−00^{d}17^{m}00^{s}9	12.2	190	11	1	1342192829	1342203587
ESO 138-G027	17^{h}26^{m}43^{s}30	−59^{d}55^{m}55^{s}6	11.1	88	6	6	1342231042	1342229216
UGC 11041	17^{h}54^{m}51^{s}82	+34^{d}46^{m}34^{s}3	10.8	74	4	5	1342231061	1342229169
IRAS 17578-0400	18^{h}00^{m}31^{s}86	−04^{d}00^{m}53^{s}3	11.2	62	8	4	1342231047	1342229187
NGC 6621	18^{h}12^{m}55^{s}31	+68^{d}21^{m}46^{s}8	11.0	92	5	4	1342221716	1342220865
IC 4687	18^{h}13^{m}39^{s}63	−57^{d}43^{m}31^{s}3	11.1	73	10	3	1342192993	1342204955
IRAS F18293-3413	18^{h}32^{m}41^{s}13	−34^{d}11^{m}27^{s}5	11.5	78	11	2	1342192830	1342204954
IC 4734	18^{h}38^{m}25^{s}60	−57^{d}29^{m}25^{s}1	11.0	67	8	4	1342240013	1342229222
NGC 6701	18^{h}43^{m}12^{s}56	+60^{d}39^{m}11^{s}3	10.9	62	9	4	1342231994	1342229137
IRAS 19254-7245[a]	19^{h}31^{m}20^{s}50	−72^{d}39^{m}21^{s}8	11.8	270	7	2	1342231039	1342206210

Table 1
(Continued)

Galaxy	R.A. J2000	Decl. J2000	$\log(L_{\text{FIR}})$ $(L_\odot)$	D_L (Mpc)	n_{det}	n_{ul}	FTS ObsId	Phot ObsID
IRAS 19297-0406	$19^h32^m22^s00$	$-04^d00^m02^s0$	12.2	387	5	7	1342231078	1342230837
ESO 339-G011	$19^h57^m37^s59$	$-37^d56^m08^s5$	10.8	82	3	8	1342231990	1342230821
3C 405	$19^h59^m28^s36$	$+40^d44^m01^s9$	$\cdots$	252	2	7	1342246994	1342230853
IRAS 20087-0308	$20^h11^m23^s87$	$-02^d59^m50^s7$	12.2	480	7	3	1342231049	1342230838
IRAS 20100-4156	$20^h13^m29^s54$	$-41^d47^m34^s9$	12.4	595	6	4	1342245106	1342230817
MCG+04-48-002a	$20^h28^m35^s02$	$+25^d44^m00^s6$	10.9	65	4	6	1342221682	1342233320
NGC 6926	$20^h33^m06^s08$	$-02^d01^m38^s7$	11.0	87	4	7	1342231050	1342218992
NGC 6946	$20^h34^m52^s30$	$+60^d09^m14^s0$	9.8	5	11	1	1342243603	1342188786
NGC 6946_05	$20^h35^m12^s01$	$+60^d08^m55^s2$	9.8	5	4	8	1342224769	1342188786
IRAS 20414-1651	$20^h44^m18^s21$	$-16^d40^m16^s2$	12.0	392	3	8	1342243623	1342231345
3C 424	$20^h48^m12^s03$	$+07^d01^m17^s5$	$\cdots$	586	0	9	1342255797	1342244149
IC 5063[a]	$20^h52^m02^s10$	$-57^d04^m06^s6$	10.2	46	3	8	1342242619	1342206208
CGCG 448-020[a]	$20^h57^m24^s33$	$+17^d07^m38^s3$	11.7	161	10	2	1342221679	1342233327
ESO 286-IG019	$20^h58^m26^s79$	$-42^d39^m00^s6$	11.8	185	11	1	1342245107	1342230815
ESO 286-G035	$21^h04^m11^s13$	$-43^d35^m34^s1$	10.8	73	7	5	1342216901	1342230813
3C 433	$21^h23^m44^s60$	$+25^d04^m27^s1$	$\cdots$	465	0	9	1342245864	1342234675
NGC 7130	$21^h48^m19^s50$	$-34^d57^m04^s7$	11.1	69	12	1	1342219565	1342210527
NGC 7172	$22^h02^m01^s91$	$-31^d52^m11^s3$	10.2	36	4	7	1342219549	1342209301
ESO 467-G027	$22^h14^m39^s85$	$-27^d27^m50^s5$	10.8	74	2	8	1342245108	1342245428
IC 5179	$22^h16^m09^s13$	$-36^d50^m36^s6$	10.9	48	6	4	1342245109	1342244158
NGC 7331	$22^h37^m04^s10$	$+34^d24^m56^s0$	10.3	15	6	4	1342245871	1342189532
UGC 12150	$22^h41^m12^s19$	$+34^d14^m56^s2$	11.1	96	6	5	1342221699	1342220870
IRAS 22491-1808	$22^h51^m49^s26$	$-17^d52^m23^s5$	11.9	345	9	2	1342245082	1342234671
NGC 7465	$23^h02^m00^s96$	$+15^d57^m53^s4$	9.7	30	3	8	1342245869	1342234763
NGC 7469	$23^h03^m15^s62$	$+08^d52^m26^s4$	11.3	72	13	0	1342199252	1342196915
ESO 148-IG002	$23^h15^m46^s72$	$-59^d03^m15^s1$	11.8	193	11	1	1342245110	1342209299
IC 5298	$23^h16^m00^s64$	$+25^d33^m23^s7$	11.3	122	7	5	1342221700	1342234766
NGC 7552	$23^h16^m10^s77$	$-42^d35^m05^s4$	10.7	21	12	1	1342198428	1342210528
NGC 7591	$23^h18^m16^s26$	$+06^d35^m08^s8$	10.8	72	6	7	1342257346	1342234758
NGC 7592[a]	$23^h18^m22^s08$	$-04^d24^m57^s6$	11.1	106	7	4	1342221702	1342234750
NGC 7582	$23^h18^m23^s50$	$-42^d22^m14^s0$	10.5	21	11	2	1342209280	1342210529
IRAS 23230-6926	$23^h26^m03^s62$	$-69^d10^m18^s8$	12.1	482	6	4	1342246276	1342230806
NGC 7674	$23^h27^m56^s68$	$+08^d46^m43^s6$	11.2	130	5	7	1342245858	1342234929
IRAS 23253-5415	$23^h28^m06^s10$	$-53^d58^m31^s0$	12.1	595	4	6	1342246277	1342234737
NGC 7679a[a]	$23^h28^m46^s61$	$+03^d30^m41^s8$	10.8	75	6	7	1342221701	1342234755
IRAS 23365+3604	23h39m01.27s	$+36^d21^m08^s7$	12.0	290	7	5	1342224768	1342234919
NGC 7771	$23^h51^m24^s88$	$+20^d06^m42^s6$	11.1	63	10	3	1342212317	1342199379
Mrk331	$23^h51^m26^s80$	$+20^d35^m09^s9$	11.2	81	12	0	1342212316	1342234682

Notes. n_{det} and n_{ul} indicate the number of 3σ detections and upper limits, respectively, reported in Table 2 out of our 13 fitted lines: CO $J = 4-3$ to $J = 13-12$, two [C I] lines, and one [N II] line.

[a] Photometry correction was not performed on the extended FTS spectrum, see Section 2.2.

(This table is available in machine-readable form.)

2. OBSERVATIONS

We compiled a list of successful extragalactic SPIRE FTS proposals (301 spectra) and searched the *Herschel* Science Archive (HSA) for the available data. In some cases, programs for higher or unknown redshift galaxies did not result in spectra with measurable CO emission, so those observations (about 74) are not presented. Table 1 lists the basic galaxy information and observation IDs for all galaxies for which at least one FTS line measurement or upper limit is reported.[6]

2.1. Herschel *SPIRE Photometry and FTS Spectra*

All spectra used in the sample were reprocessed with HIPE[7] developer's version 13.0.3849 and `spire_cal_13_0`, obtained from Rosalind Hopwood on 2014 September 30. This calibration corrects for rapidly changing telescope temperatures near the beginning of observation cycles, which has the largest effect on faint sources (Swinyard et al. 2014). Overall the calibration errors, even from earlier calibration sets, are within 6% for point sources and 7% for extended sources. The majority of the observations were performed in sparse sampling mode, for which we took the spectra from the central pixels (SLWC3, SSWD4). For those mapping observations in the intermediate or fully sampled modes, we extracted the

---

[6] The spectra for this survey came from the following programs, with the total number of observations presented in Table 1 in parentheses: OT1_nlu_1 (92), KPOT_pvanderw_1 (31), OT1_dfarrah_1 (28), OT1_jsmith01_1 (23), OT1_pogle01_1 (13), KPGT_cwilso01_1 (12), OT1_lyoung_1 (8), GT1_lspinogl_2 (10), OT1_pvanderw_4 (5), GT2_vleboute_3 (2), OT2_vkulkarn_3 (2), KPGT_rguesten_1 (1), OT1_dmarrone_1 (0), OT1_rivison_1 (0), OT2_drigopou_3 (0), and OT2_rivison_2 (0).

[7] HCSS, HSpot, and HIPE are joint developments by the Herschel Science Ground Segment Consortium, consisting of the ESA, the NASA Herschel Science Center, and the HIFI, PACS and SPIRE consortia.

spectrum from the pixel corresponding to the central coordinates of the map (those in Table 1). All SPIRE photometry was downloaded in 2014 September from the HSA (SPG v11.1.0) and not reprocessed.

2.2. Source/Beam Correction

The majority of the sources in our band are quite point-like compared to the SPIRE FTS beam, which varies from ~45″ to 17″. Because the beam size is discontinuous between the upper frequency end of the SLW band and the lower frequency end of the SSW band, galaxies which are not point-like will show a notable discontinuity at this juncture. Even galaxies that are relatively small compared to the beam, but still not perfectly point-like, will show this discontinuity and require a correction to properly compare the emission across the SPIRE bandpass. This is necessary because we only use the central FTS detectors. An example is shown in Appendix.

We perform the same source/beam correction as described in full detail in Section 2.2 of K14. Briefly, we use the SPIRE Photometer Short Wave (PSW, 250 μm) maps, observed with 19″32 beams, convolve them to larger beam sizes (Ω_b), and measure the new peak flux density. We compare this flux density to that of a $b = 43$″5 beam, which corresponds to the beam at the CO $J = 4-3$ transition. The ratio of the two flux densities, $\eta_{b,43.5}$, as a function of beam size, is between that expected for a point source (1) and a fully extended source ($\Omega_b/\Omega_{43.5}$). For each galaxy's unique distribution, for any beam size, we have a value of $\eta_{b,43.5}$ to refer the emission to a 43″5 beam. We divide the SPIRE spectrum by $\eta_{b,43.5}$ to refer the flux density at all wavelengths to that observed by a 43″5 beam. We also use these values to refer CO integrated flux values measured from other facilities with smaller beam sizes to the 43″5 beam (Section 2.4).

We apply an additional correction (also used in K14) to match the total flux density of the spectrometer with the photometer flux density. At the high frequency end, we match the total SSW flux density integrated over the photometer PSW bandpass, $\hat{F}(PSW)$, to that of the PSW photometer-integrated flux density at 43″5, $F''(PSW)$ by multiplying the spectrum by $X_{SSW} = F''(PSW)/\hat{F}(PSW)$. There are two photometer bands (PMW and PLW) which overlap with the SLW band, so we define a line that connects those two ratios, $F''(PMW)/\hat{F}(PMW)$ and $F''(PLW)/\hat{F}(PLW)$, and multiply the spectrum by that ratio as a function of wavelength, X_{SLW} (ν). This photometry correction step is often most significant in the SSW, which can overestimate the measured flux compared to the photometry. Some spectra had somewhat over-subtracted telescope emission, giving slightly negative flux densities, in particular at the lowest-frequency end. In these cases, no correction was applied to the SLW band to match the PLW photometry, which would use negative ratios. In a few cases, we also did not correct the SLW band if the ratios derived from the PLW and PMW were significantly discrepant (i.e., would produce a nonsensical SLW continuum). The spectra that were not corrected are marked in Table 1.

In order to compare the CO emission to L_{FIR}, we must also correct L_{FIR} to properly represent the same amount of emission as the CO within our beam. Similar to the procedure above, we convolve the SPIRE photometer maps at wavelength λ to the beam size of 43″5 and find the ratio of the peak flux density in Jy measured with such a beam ($F_{beam,\lambda}$) to the total integrated emission in the map ($F_{total,\lambda}$). Assuming $L_{FIR,beam} =$

$L_{FIR,total} \times F_{beam,250\,\mu m}/F_{total,250\,\mu m}$, and likewise for the 350 and 500 μm maps, we can determine the proper $L_{FIR,beam}$ for comparison to the CO emission. The three photometers agreed well, and so we use the average of the $F_{beam,\lambda}/F_{total,\lambda}$ ratios. Of the 232 observations with known redshift and available spectra, 118 have ratios of <0.8, and 42 have ratios of <0.5. We propagate the errors from the total measured integrated flux density through to the final measurement of $L_{FIR,beam}$.

2.3. Herschel FTS Line Fitting Procedure

The CO $J = 4-3$ to $J = 13-12$ lines, both [C I] lines, and the [N II] 205 μm line are the brightest lines in the FTS spectra. To fit these, we start with the FTFitter code from the University of Lethbridge.[8] Treating each detector (SLW and SSW) separately, the code fits a polynomial to the baseline, and then simultaneously fits unresolved lines at the expected frequencies of the lines listed above (given known redshifts). We place the lower limit of the total area of the line profile to be above 0; we do not expect any of these lines to be in absorption. We limit the line center to within ± 500 km s^{-1} of that expected from the redshift to allow for uncertainty in the velocity scale and physical differences in the gas kinematics. In wavenumbers, this is about 0.025–0.084 cm^{-1} over the band, compared to the FWHM of the line profile of 0.048 cm^{-1}.

We manually inspected the resulting fits to determine if any lines were clearly resolved. This is most likely to be the case for the [N II] line as its velocity resolution is the highest at the higher frequencies, and it is much brighter than the CO lines at similarly high frequencies which may be undetected. Resolved lines do not show the same characteristic ringing of the sinc function; the ringing is significantly lower, if not imperceptible, smeared out by the effective convolution of the emission line profile and instrumental profile. We refit the lines that meet this criteria as a Gaussian convolved with the instrumental line profile. In this case, the lines are barely resolved, thus Gaussian profiles are perfectly adequate (no more detailed velocity profiles can be determined from the FTS).

The fact that SPIRE utilizes a FTS introduces a special problem in the treatment of line fitting. The true measured quantity is the interferogram, or the interference pattern at the focus as a function of optical path difference (OPD) as the mirror of the interferometer moves linearly. The spectrum itself is the Fourier transform (FT) of this interferogram, which leads to two important consequences: (1) the wavelength bins are not truly independent, which many fitting routines assume, and (2) the resulting noise pattern closely resembles the FWHM = 0.048 cm^{-1} sinc function line profile. The result is that the errors output by a least-squares fitter, like the FTFitter and the built-in HIPE Spectrum Fitter routines, may not be an accurate representation of the line flux uncertainty. Moreover, it can do an excellent job of fitting a "ripple" in the spectrum which, to the observer's eye, may not be particularly distinguishable from any other ripple nearby, other than that we expect the, e.g., CO line to correspond to the fitted ripple's wavelength, and no similarly strong lines to be adjacent in the spectrum.

Although the ideal situation would be to the fit the interferogram itself,[F] this is not a user-accessible option for SPIRE data considering the many calibration steps that occur in processing after the FT. Instead, we created a Bayesian analysis

---

8 https://uleth.ca/phy/naylor/index.php?page=ftfitter

Table 2
Line Fluxes and Uncertainty Ranges from SPIRE FTS

Galaxy	Line	Resolved?	Median (Jy km s^{-1})	-1σ (Jy km s^{-1})	$+1\sigma$ (Jy km s^{-1})	3σ Upper Limit (Jy km s^{-1})
NGC 0023	CI1-0	⋯	2.57e+02	6.81e+01	5.57e+02	7.98e+02
NGC 0023	CI2-1	⋯	3.82e+02	3.09e+02	4.57e+02	⋯
NGC 0023	CO4-3	⋯	3.12e+02	7.15e+01	6.10e+02	1.21e+03
NGC 0023	CO5-4	⋯	7.38e+02	5.76e+02	9.69e+02	⋯
NGC 0023	CO6-5	⋯	4.23e+02	3.26e+02	4.88e+02	⋯
NGC 0023	CO7-6	⋯	3.24e+02	2.42e+02	3.97e+02	⋯
NGC 0023	CO8-7	⋯	2.49e+02	1.18e+02	3.83e+02	5.71e+02
NGC 0023	CO9-8	⋯	1.15e+02	2.51e+01	2.94e+02	5.63e+02
NGC 0023	CO10-9	⋯	2.22e+02	5.53e+01	3.56e+02	5.28e+02
NGC 0023	CO12-11	⋯	7.78e+01	1.81e+01	1.92e+02	3.26e+02
NGC 0023	CO13-12	⋯	2.29e+02	9.69e+01	3.55e+02	4.76e+02
NGC 0023	NII	X	2.63e+03	2.46e+03	2.80e+03	⋯
NGC 34	CI1-0	⋯	4.96e+02	3.36e+02	6.45e+02	⋯
NGC 34	CI2-1	⋯	4.29e+02	3.83e+02	4.72e+02	⋯
NGC 34	CO5-4	⋯	7.87e+02	6.92e+02	8.77e+02	⋯

(This table is available in its entirety in machine-readable form.)

method to determine the probability distribution function (PDF) of the true line flux given the observed line flux, $P(f_{\rm true}|f_{\rm obs})$, which is heavily influenced by the correlated noise pattern in the spectrum. The noise itself is difficult to accurately characterize, varying from observation to observation, and across the bandpass of a given observation. Therefore, instead of attempting to describe the correlated noise for our entire sample, we focus on the area around each individual (unresolved) line.

We describe the procedure briefly here, but show a more in-depth example with illustrative figures for NGC 4388 in the Appendix. This procedure is not used for lines that were manually identified as resolved, which already have a high signal-to-noise ratio (S/N). For each line, we input sinc profile lines of varying amplitudes $f_{\rm true}$ over the region $\pm 2\,{\rm cm}^{-1}$ from the line center (excluding the area immediately around any CO, [C I], or [N II] lines) and then refit the spectrum. We compare the measured integrated fluxes, $f_{\rm obs}$ to the known input values, $f_{\rm true}$. The PDF for our CO line is the distribution of the input fluxes that produced that particular measured flux value, a slice of the $P(f_{\rm obs}|f_{\rm true})$ two-dimensional distribution that we created.

For high S/N line detections, the procedure replicates a Gaussian distribution of similar median and error (σ) as the parameters estimated by the FTFitter. This is because a very high amplitude line input, added anywhere in the spectrum, will return the same integrated flux value as we input ($f_{\rm obs} = f_{\rm true}$). However, a line with smaller amplitude may add constructively or destructively to the underlying ripple pattern of the spectrum, returning a higher or lower flux than input. A local variation from the detector's average baseline may also influence the final fitted value, which may shift the median value of the PDF of the line flux.

The procedure makes the most difference for the high-J CO lines; 60% of the 3σ detections of CO $J = 13-12$ from least-squares fitting were shown to have $>3\sigma$ uncertainty. For all the CO lines in the SSW band ($J_{\rm upper} \geqslant 9$), this number is 44%. For the CO lines in the SLW band, it is only 15%. The numbers are the lowest for [N II] (4%) because it is so bright, and for [C I] $J = 2-1$ and CO $J = 7-6$ (5%, 8%) because they lie in the lowest noise part of the spectrum and are relatively bright.

The results from this line fitting procedure are shown in Table 2. The median, -1σ, and $+1\sigma$ values are derived from the points at which the cumulative distribution functions (CDFs) equal 0.5, 0.159, and 0.841, respectively. If $-1\sigma/$ median is less than 3, a value for a 3σ upper limit is also shown (where CDF = 0.997).

2.4. Low-J CO Lines from the Literature and ARO

The bandpass of the *Herschel* FTS starts around the CO $J = 4-3$ line, but the majority of the molecular mass in galaxies is cool and populates the lower rotational levels. We complement the line fluxes derived from the FTS with the CO $J = 1-0$, $J = 2-1$, and $J = 3-2$ lines available from ground-based observatories. Many of these galaxies have already been studied in the literature, particularly in large CO surveys.

For some galaxies, we also performed single-dish measurements using the ARO. Measurements of the CO $J = 1-0$ line were conducted with the 12 m dish on Kitt Peak in 2015 May, and those of CO $J = 2-1$ and $J = 3-2$ were conducted with the Submillimeter Telescope (SMT) located on Mt. Graham from 2014 November to 2015 February. At the 12 m, we used the ALMA Type 3 mm receiver with two 2 MHz backends in series, yielding a 2.6 km s^{-1} channel resolution and an about 670 km s^{-1} bandwidth. At the SMT, we used the ALMA Type 1.3 mm sideband separating receiver (for CO $J = 2-1$) and the 0.8 mm double sideband receiver (for CO $J = 3-2$) with the 1 MHz filterbanks in 2IF mode. Most observations were conducted with beam switching, except for highly extended sources which required position switching. Pointing and focus were checked periodically on planets or bright continuum sources.

Beam efficiency measurements were conducted with Venus and Jupiter[9] using the procedure described in Schlingman et al. (2011). For CO $J = 1-0$, $J = 2-1$, and $J = 3-2$ we found $\eta_{\rm mb}$ of 0.86–0.89, 0.57–0.62, and 0.58–0.65, respectively. The beam sizes are approximately 55″, 32″, and 22″, respectively. The spectra were reduced, baseline subtracted, and converted to the $T_{\rm mb}$ scale using $\eta_{\rm mb}$ in CLASS. Finalized spectra were

---

[9] Additional planetary observations provided by Karin Sandstrom.

Table 3
CO $J = 1−0$ to $J = 3−2$ Line Fluxes

Galaxy	J_{up}	Reported	σ_m	σ_c	Unit $\times$ km s^{-1}	Δ_v	Ω_b	$I\Delta_v$ (Ω_{FTS})	σ	References
NGC 0023	1	16.9	⋯	4.2	K	141	24	138.9	34.7	(1)
NGC 0023	1	6.0	⋯	1.2	K	374	55	169.9	34.0	(2)
NGC 0023	1	8.9	⋯	2.2	K	190	45	184.4	46.1	(1)
NGC 0023	1	18.0	⋯	1.3	K	⋯	33	234.0	16.9	(3)
NGC 0023	1	34.0	0.4	6.8	K	⋯	22	247.4	49.6	(4)
NGC 0023	2	18.8	⋯	4.7	K	129	12	235.6	58.9	(1)
NGC 0023	2	7.4	⋯	1.9	K	210	24	243.2	60.8	(1)
NGC 0023	3	15.3	1.3	2.3	K	257	22	1003.0	171.8	(5)
NGC 34	1	17.0	⋯	4.2	K	149	24	115.3	28.8	(1)
NGC 34	1	4.5	0.3	0.4	K	295	55	131.8	16.0	(6)
NGC 34	1	6.7	⋯	1.7	K	274	45	138.4	34.6	(1)
NGC 34	1	148.5	13.5	29.7	Jy	⋯	45	147.6	32.4	(7)
NGC 34	2	4.3	⋯	1.1	K	271	24	116.7	29.2	(1)
NGC 34	2	56.5	⋯	14.1	K	172	12	471.9	118.0	(1)
NGC 34	3	7.7	1.8	1.2	K	168	22	404.8	110.5	(5)

Note. The first eight columns refer specifically to the measurements reported in the literature. "Reported" is the reported value in the units of the "Unit" column. σ_m and σ_c refer to measurement and calibration error, if separately reported, otherwise calibration errors are assumed or contain total error. Δ_v is the FWHM of the line, if reported, and Ω_b is the FWHM of the beam size. The next two columns are the values used in our analysis: $I\Delta_v$ (Ω_{FTS}) is the flux in Jy km s^{-1}, referred to the 43$''$5 beam, and σ is the total accompanying error.

References. (1) Albrecht et al. 2007; (2) Sanders et al. ;1991; (3) Elfhag et al. 1996; (4) García-Burillo et al. 2012; (5) SMT (this work); (6) Maiolino et al. 1997; (7) Baan et al. 2008; (8) 12 m (this work); (9) Leroy et al. 2006; (10) Bayet et al. 2006; (11) Mao et al. 2010; (12) Mirabel et al. ;1990; (13) Garay et al. 1993; (14) Harrison et al. 1999; (15) Young et al. 1995; (16) Earle 2008; (17) Solomon et al. 1997; (18) Papadopoulos et al. 2012; (19) Evans et al. 2005; (20) Aalto et al. 1995; (21) Leech et al. 2010; (22) Kamenetzky et al. 2011; (23) Spinoglio et al. 2012; (24) Young et al. 2011; (25) Alatalo et al. 2011; (26) Lazareff et al. 1989; (27) Papadopoulos & Seaquist 1998; (28) Sandqvist et al. 1995; (29) Sandqvist 1999; (30) Bothwell et al. 2013; (31) Ward et al. 2003; (32) Yao et al. 2003; (33) Sliwa et al. 2012; (34) Boselli et al. 2014; (35) Schirm et al. 2014; (36) Wild & Eckart 2000; (37) Eckart et al. 1990; (38) Mauersberger et al. 1999; (39) Greve et al. 2009; (40) Claussen & Sahai 1992.

(This table is available in its entirety in machine-readable form.)

smoothed to approximately 20 km s^{-1} bins from which the total integrated fluxes were derived.

All low-J lines utilized in this work, including the ones from ARO, are available in Table 3. As Table 3 shows, the low-J lines we use come from a variety of telescopes with different beam sizes. For subsequent comparison to *Herschel* CO lines, all line fluxes are referenced to the 43$''$5 beam size using the same ratios ($\eta_{b,43.5}$) as described in Section 2.2. Table 3 lists both the literature reported values (third column, in their original beam sizes and units) and the 43$''$5 referenced fluxes in Jy km s^{-1} we use in our analysis (ninth column).

3. ANALYSIS

We examined the relationship between L'_{CO}[10] and L_{FIR} (from 40–120 μm), similar to Lu et al. (2014), Greve et al. (2014), and Liu et al. (2015), discussed further in Section 3.2. We chose the orientation of our axes, with L_{FIR} on the y-axis, for the easiest comparison to the existing literature. This orientation comes from the comparison to the K–S scaling law, which relates the SFR (y-axis) to molecular gas surface density (x-axis), with $\dot{\Sigma}_* \propto \Sigma_{gas}^{1.4\pm0.15}$ (Kennicutt 1998). Subsequent large-scale analyses have found indices from 1.0 to 1.4 for the molecular gas and higher values, 1.4–3.1, for the total gas surface density (Kennicutt & Evans 2012). L_{FIR} can be considered a proxy for the SFR if one excludes the contribution

of active galactic nuclei (AGNs) to L_{FIR}, which we admittedly do not separate here. It is likely small for most sub-ultraluminous infrared galaxies (ULIRGs), especially at these wavelengths. In the case of $J = 1−0$, the well-known "X-factor" or α_{CO} is used to relate the luminosity of CO $J = 1−0$ to the total molecular mass, so the slope derived here is comparable to the K–S relation. However, this relationship is not applicable at higher-J, where the CO luminosity is not a tracer of mass (K14), but we choose to keep the same orientation to avoid confusion. Neither variable should be considered the "independent" one, regardless of which appears on the x-axis.

The theoretical explanations for these relationships were first investigated to describe the discrepant power laws in low-J emission of various molecules, namely CO $J = 1−0$, where $L_{FIR} \propto L_{CO}^{1.4-1.6}$ and HCN $J = 1−0$, where $L_{FIR} \propto L_{HCN}^{1.0}$ (Gao & Solomon 2004a, 2004b). The CO slope closely resembles that of the aforementioned K–S relation slope, but HCN does not match. Krumholz & Thompson (2007) showed that this could be understood as a consequence of the different critical densities for different species' ground-state transitions, assuming isothermality. In short, a molecular line with a low critical density compared to a galaxy's median gas density, ρ_g, will be excited by the majority of the molecular gas. The SFR will therefore depend on one factor of density ρ_g based on the total amount available for SF, and a factor $\rho_g^{0.5}$ from the dynamical timescale of the gas, adding up to a total factor of 1.5 in the case of the low-n_{crit} CO $J = 1−0$ line. On the other hand, when the molecular line has a critical density higher than that of the median gas density, its emission will be picked out from high-density peaks only, specifically peaks of the same density (and

---

[10] $L'_{CO} = 3.25 \times 10^7 S_{CO} \Delta v D_L^2 (1 + z)^{-3} \nu_{obs}^{-2}$ [K km s^{-1} pc^2], where D_L is the luminosity distance in Mpc, ν_{obs} is in GHz, and $S_{CO}\Delta v$ is in Jy km s^{-1} (from Carilli & Walter 2013; Solomon et al. 1992). Note that L'_{CO} is just the area within the beam times the velocity-integrated antenna temperature, $A \times T\Delta v$, where A is the area $10^{12}\Omega D_L^2 (1 + z)^{-4}$ [pc^2].

Table 4
Correlations between L'_{CO} and L_{FIR}: Full Sample

J_{up}	a	σ_a	b	σ_b	n
1	1.27	0.04	−1.0	0.4	299
2	1.11	0.07	0.6	0.7	138
3	1.18	0.03	0.1	0.3	131
4	1.09	0.05	1.2	0.4	108
5	1.05	0.03	1.8	0.3	195
6	1.04	0.03	2.2	0.2	199
7	0.98	0.03	2.9	0.2	196
8	1.00	0.03	3.0	0.3	186
9	1.03	0.04	2.9	0.3	176
10	1.01	0.03	3.2	0.3	184
11	1.06	0.04	3.1	0.3	166
12	0.99	0.03	3.7	0.2	168
13	1.12	0.04	2.9	0.3	156

Note. Best-fit measurements and errors for $\log(L_{FIR}) = a \log(L'_{CO}) + b$. Column $n =$ number of data points used in relation (not all 3σ detections).

Table 5
Correlations between L'_{CO} and L_{FIR}: AGNs Only

J_{up}	a	σ_a	b	σ_b	n
1	1.54	0.07	−3.4	0.7	99
2	1.24	0.14	−0.6	1.2	39
3	1.30	0.08	−1.1	0.7	39
4	1.15	0.08	0.6	0.6	33
5	1.15	0.04	0.9	0.3	60
6	1.09	0.04	1.6	0.4	62
7	1.03	0.04	2.5	0.3	61
8	1.03	0.05	2.6	0.4	58
9	1.02	0.06	2.9	0.5	53
10	1.01	0.05	3.1	0.4	58
11	1.01	0.07	3.3	0.5	56
12	0.99	0.06	3.6	0.4	55
13	1.13	0.07	2.7	0.5	53

Note. Best fit measurements and errors for $\log(L_{FIR}) = a \log(L'_{CO}) + b$. Column $n =$ number of data points used in relation (not all 3σ detections).

therefore the same free-fall time) across different galaxies. Therefore the higher n_{crit} of HCN $J = 1-0$ yields a slope of 1.0. We discuss our results in context of these expectations in Section 4.

3.1. Fitting L'_{CO}/L_{FIR} Slopes

As mentioned in Section 2.2, all fluxes including L_{FIR} are referred to the emission within a $43''\!.5$ beam. To determine the coefficients of the relation $\log(L_{FIR}) = a \log(L'_{CO}) + b$, we used the python module lnr.bces[11], which utilizes the Bivariate Correlated Errors and intrinsic Scatter method of Akritas & Bershady (1996). This is important because we have errors on both variables (we introduced a non-negligible error into the L_{FIR} variable through our source/beam correction). As stated above, we chose the examination of L_{FIR} as a function of L'_{CO} to match the most recent literature and note that the solution to the inverse problem (L'_{CO} as a function of L_{FIR}) does not simply produce best-fit slopes that are the inverse of those presented here. For the case of low-J lines collected from the literature and our ARO follow-up, multiple measurements for the same galaxies (positioned at the location matching the FTS coordinates) are treated independently.

When including all spectra in our sample, we find slopes starting at 1.3 for CO $J = 1-0$, and lowering to about ~1 for the mid- to high-J CO lines, with no discernible trend with increasing J. The results are shown in Table 4. There is no significant difference whether we include or exclude FTS lines with S/N < 3. We also separated our samples into a few categories that are somewhat overlapping, and summarize the differences here:

1. We separated our galaxies into known AGN (categorized in Hyperleda[12] as a quasar or any type of Seyfert galaxy) or not. This classification (using the agnclass category) is taken from the Véron-Cetty & Véron (2006) catalog. Within those classified by Hyperleda as AGNs (78 of the 232 galaxies), no information is provided regarding the relative SF versus AGN contributions to the total L_{FIR}, so this is a somewhat crude

Table 6
Correlations between L'_{CO} and L_{FIR}: (U)LIRGs Only

J_{up}	a	σ_a	b	σ_b	n
1	1.15	0.09	0.2	0.8	225
2	0.66	0.15	4.9	1.4	100
3	0.94	0.11	2.3	1.1	86
4	0.68	0.13	4.9	1.1	44
5	0.96	0.07	2.7	0.6	129
6	1.02	0.05	2.4	0.4	132
7	0.92	0.04	3.5	0.4	131
8	0.91	0.04	3.7	0.3	125
9	0.92	0.07	3.8	0.5	111
10	0.83	0.03	4.7	0.3	126
11	0.86	0.05	4.7	0.4	115
12	0.79	0.04	5.3	0.3	114
13	0.85	0.05	5.0	0.4	109

Note. Best fit measurements and errors for $\log(L_{FIR}) = a \log(L'_{CO}) + b$. Column $n =$ number of data points used in relation (not all 3σ detections).

Table 7
Correlations between L'_{CO} and L_{FIR}: Non-(U)LIRGs Only

J_{up}	a	σ_a	b	σ_b	n
1	1.05	0.09	0.8	0.8	74
2	1.12	0.11	0.4	0.9	38
3	1.05	0.05	0.9	0.4	45
4	1.09	0.07	1.2	0.5	64
5	1.01	0.06	2.1	0.5	66
6	1.01	0.05	2.3	0.4	67
7	1.00	0.06	2.8	0.4	65
8	1.07	0.07	2.5	0.5	61
9	1.06	0.08	2.7	0.5	65
10	1.12	0.07	2.5	0.5	58
11	1.10	0.09	2.7	0.6	51
12	1.03	0.07	3.4	0.4	54
13	1.23	0.08	2.2	0.5	47

Note. Best fit measurements and errors for $\log(L_{FIR}) = a \log(L'_{CO}) + b$. Column $n =$ number of data points used in relation (not all 3σ detections).

division of the galaxy sample. Looking only at AGNs (Table 5), compared to the whole sample we find higher slopes for the low-J lines (1.5 ± 0.1, 1.2 ± 0.1, 1.3 ± 0.1,

---
[11] http://home.strw.leidenuniv.nl/~sifon/pycorner/bces/, by Cristóbal Sifón.
[12] http://leda.univ-lyon1.fr/leda/rawcat/a109.html

1.1 ± 0.1, 1.15 ± 0.04 for $J = 1-0$ through $J = 5-4$), but the slope error bars overlap by CO $J = 6-5$ and continue to follow the same trend as the whole sample. Looking at the sample that completely excludes AGNs, we find a lower slope than the whole sample for CO $J = 1-0$ (1.13 ± 0.06), but at subsequently higher-J the slopes are not distinguishable from the combined sample. In summary, comparing the AGN to the non-AGN sample, the most significant difference is in the CO $J = 1-0$ line. There are also differences, at less significance, up to the $J = 5-4$ line. The low-J CO emission is not expected to be affected by the AGN; the L_{FIR} and high-J CO are likely being influenced. We likely do not see any difference because our AGN-designated galaxies (which are only about one third of the full sample) may not be entirely dominated in their molecular excitation from the AGN; as mentioned, we do not separate the relative SF versus AGN contributions to total L_{FIR}. Better quantification of the AGN influence, and higher spatial resolution, may result in differences in the slope.

2. Astronomers often separate galaxies into (U)LIRGs or lower luminosity galaxies. We separate our galaxies at $L_{FIR} = 6 \times 10^{10} L_\odot$ which we found is approximately equal to $L_{IR}(8-1000\,\mu m) = 1 \times 10^{11}$, based on the luminosities listed in Greve et al. (2014) and K14. (The exact cutoff value does not change the conclusions that follow.) The CO $J = 1-0$ line has been known to not be fit by one slope among (U)LIRGs and lower luminosity galaxies; the superlinear slope that results from a single power line fit is due to higher dense gas fractions in (U)LIRGs (Gao & Solomon 2004b; Greve et al. 2014), essentially creating a higher intercept (but the same slope). We do find lower slopes in $J = 1-0$ among these two populations fit separately than their combined slope of 1.3 ± 0.4. We find that the mid-J lines of CO are well fit by a single slope across many orders of magnitude; the slopes in all three cases (full sample; just (U)LIRGs; just galaxies with lower luminosities than (U)LIRGs) are not statistically distinguishable given the error bars. Our three highest-J CO lines ($J = 11-10$, $J = 12-11$, $J = 13-12$), however, do show a measurable difference in the best-fit slope. Focusing primarily on (U)LIRGs changes the slopes at higher-J, decreasing to about 0.83 ± 0.03 (weighted average of the three highest-J CO lines in Table 6), a highly significant difference from 1. The results for these two populations are shown in Tables 6 and 7.

3. We restricted the fit to only those galaxies that are not particularly well resolved, those with $L_{FIR,beam} \geqslant 0.8$ $L_{FIR,total}$ based on the photometry maps, to see if our infrared luminosity correction could be influencing the y-axis values. We find lower slopes in this case, 0.88 ± 0.06 on average for high-J lines, but this may be due to the fact that $2/3$ of this population are (U)LIRGs, not because large L_{FIR} corrections are necessarily inaccurate.

Certainly, these slopes are masking a considerable amount of scatter in the data, and different trends can be discerned when fitting different populations (also seen in Liu et al. 2015). The remaining figures of this paper examine the survey populations themselves with comparisons to these derived, "global" relations.

Fitting a linear relation in log space requires creating error bars that are symmetric in log space, which ours are not. The exaggeration of the linear errors when viewed in log space is highest for those line measurements with the lowest S/N. To test whether the conversion to these symmetric error bars (which decreases the size of the lower error bar) introduces systematic bias in deriving the slopes, we chose fixed values of the slopes, set the nominal y-values to match the chosen slope, and draw randomly from each data point's x and y error bars in linear space. Fitting such scattered distributions many times results in distributions centered upon the chosen slopes and with scatter comparable to our error bars in Table 4. We find no evidence of systematic bias due to this effect.

We also investigated whether our error bars are responsible for the slightly lower value of the CO $J = 1-0$ line's slope at 1.3 instead of 1.4–1.6. This value is not due to the error bars in either the x- or y-directions; we still find a slope of about 1.3 if we exclude one, the other, or both in the line fitting. We do find a slope of 1.44 if we restrict the fit to those data points with log $(L'_{CO}) > 9$, indicating that the lower luminosity points are bringing down the slope overall.

3.2. Comparison to Similar Works

Greve et al. (2014) conducted a comparison of CO emission to L_{FIR} for the non-extended galaxies of the HerCULES sample (van der Werf et al. 2010) and found sharply decreasing slopes between log(L_{FIR}) and log(L'_{CO}), starting around 1 at CO $J = 1-0$ and decreasing as one moves to higher-J starting around CO $J = 6-5$ (0.93 ± 0.05, down to 0.47 ± 0.20 by the $J = 13-12$ line).

They interpret this sublinear slope as an indication that far-UV (FUV) radiation fields are not responsible for the the dense, warm gas emitting in the high-J lines. Mechanical heating and shocks are the likely explanation for the high-J excitation, as was shown in many galaxies of the sample of K14 (and references therein). We are in agreement with Greve et al. (2014) that mechanical feedback can be related to SF, such as stellar outflows, winds, and supernova remnant expansion; not being related to the FUV radiation from stars does not mean the excitation is not related to SF at all.

The fluxes used in Greve et al. (2014) are reported in Rosenberg et al. (2015). Their sample is included in ours, but our measured fluxes do not match in all cases. For lines up to $J = 10-9$, $2/3$ of their 18 non-extended galaxies match our flux values within 30%. At higher-J, this number is more like $1/3$. When discrepant, their values are often ~50% higher, or even factors of a few for IRAS F05189-2524, for which we do not use the same spectra. The major difference for other galaxies is likely the treatment of the source/beam correction. Importantly, Greve et al. (2014) only included (U)LIRGs (log $(L_{FIR}) \geqslant 11$). As discussed above, we find lower slopes if we restrict ourselves to this population, but not as low as the slopes reported for Figure 1 by Greve et al. (2014), due to the differences in our measured fluxes.

Liu et al. (2015) conducted a larger study, more comparable to ours, utilizing the full extent of the *Herschel* archive. With the inclusion of galaxies from log(L_{FIR}) $\geqslant 8$, they found linear slopes between log(L_{FIR}) and log(L'_{CO}) throughout the CO ladder starting at $J = 4-3$ (statistically consistent with our results). Also consistent with our results and Greve et al. (2014), restricting the fits to the HerCULES sample of (U)LIRGs yields sublinear slopes for the highest-J lines. Their
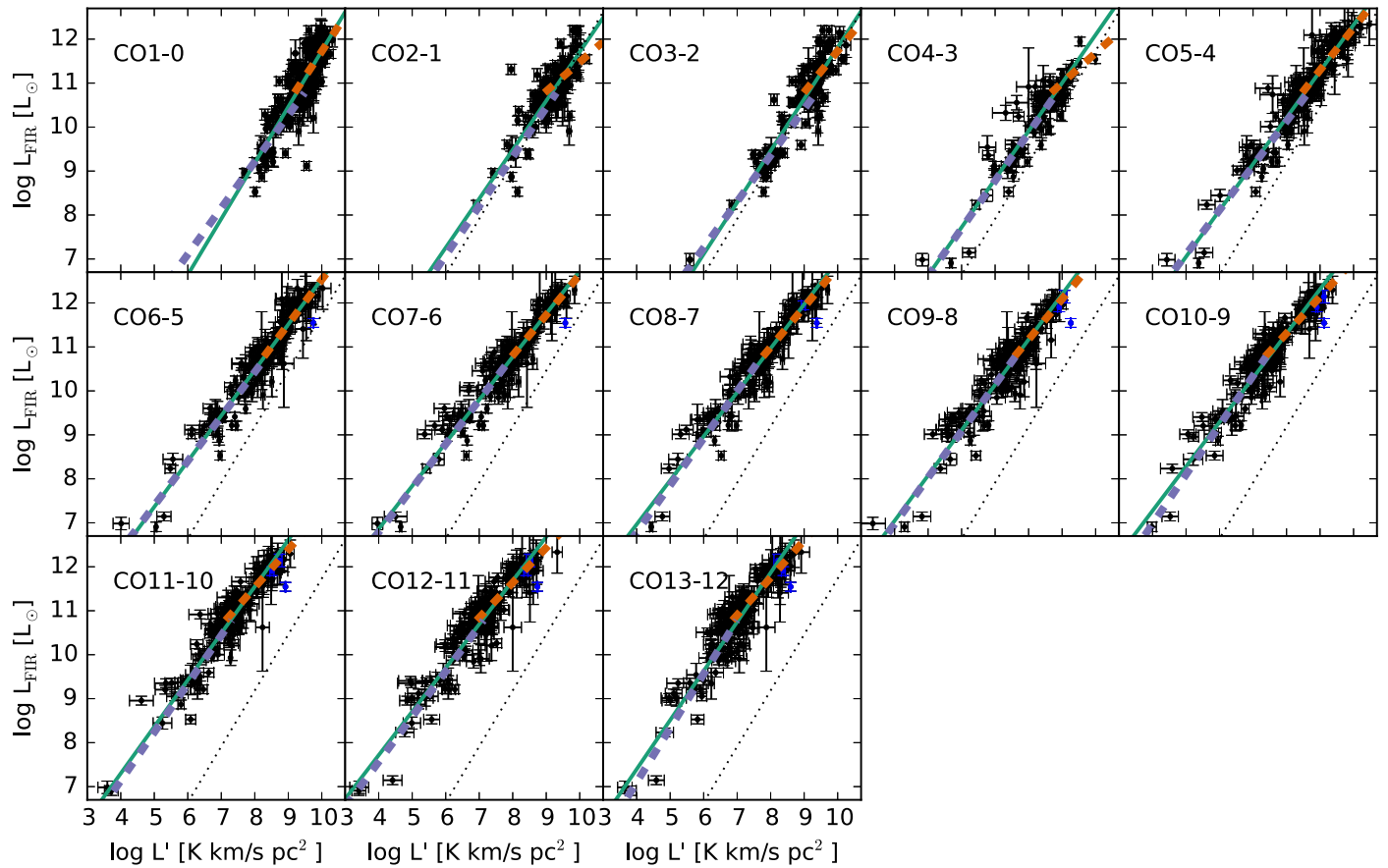
Figure 1. CO vs. L_{FIR}. The y-axis is the L_{FIR} in the beam for comparison to the CO measurement (see Section 2.2). Low-J lines may include multiple measurements for the same galaxy if available in the literature (Table 3). Blue data points indicate resolved (sinc-Gaussian) measurements from the FTS. Line fits are described in Section 3. The green line is fitting the whole sample; the CO $J = 1-0$ line fit is shown as a dotted black line on each CO plot for comparison. The dashed orange and purple lines are fits when separating the sample into galaxies above and below $L_{FIR} = 6 \times 10^{10} L_\odot$, respectively.

work does not include a table of the galaxies included in their sample or the line fluxes used, so we cannot make a direct comparison of the fluxes used for our relations at this time. Some major differences may be important in the comparison of our work: first, they use SPIRE calibration version 12 and we use version 13, which may make the most difference for galaxies observed near the start of SPIRE cooling cycles (due to "cooler burp"). Second, each of their CO and L_{FIR} relations use a different beam size, that of the frequency of the CO line in the FTS. Third, for sparsely and intermediately sampled galaxies, they extract spectra from multiple bolometers in the detector array, meaning they are including multiple spatially Nyquist-sampled data points in their relationships (with their own matching L_{FIR} values) for such galaxies. Finally, their line fitting procedure uses sinc-convolved-Gaussian (SCG) lines in HIPE for sparse observations and sinc for intermediate or full sampling observations. They note that SCG-derived fluxes are systematically higher, but we found that few galaxies have CO linewidths large enough to be resolved by the FTS. Differences in the slopes of (U)LIRGs among Liu et al. (2015), Greve et al. (2014), and this work can also be attributed to the small dynamical range spanned by (U)LIRGs. Despite these differences, our results agree well in finding mid- to high-J CO slopes of 1 in a large sample of galaxies and less than 1 for (U)LIRGs.

Lu et al. (2014) also examined the CO $J = 4-3$ through $J = 13-12$ emission of the 65 LIRGs in the Great

Observatories All-Sky LIRG Survey, comparing to the IRAS 60–100 μm color, C(60/100), as a proxy for dust temperature. They demonstrated that L_{IR} is not the best predictor of SLED shapes; we find an overall trend in Figure 2 (the line luminosity ratios relative to $J = 1-0$ in average SLEDs by L_{FIR} bin increase with L_{FIR}), but also a significant amount of variation in Figure 3 (individual mid- to high-J CO/$J = 1-0$ luminosity ratios for each galaxy, unbinned), discussed in the next section. C(60/100), which is not presented here, is potentially a better predictor of the CO SLED shape (based on the line at which the SLED peaks in luminosity).

3.3. Average SLEDs by L_{FIR} Ranges

Within galaxy-wide $\log(L_{FIR})$ ranges of approximately 0.5 dex, we compiled weighted-averaged $(L_{CO}/L_{FIR})/(L_{CO}(J = 1-0)/L_{FIR})$ ratios, presented in Figure 2 (top; see caption for note about conversion to L'_{CO}). The SLEDs are normalized to the $J = 1-0$ line to show the relative excitation across the CO ladder. The CO $J = 1-0$ line measures emission from the same type of cold, ubiquitous molecular gas found throughout many types of galaxies. There are four main trends to examine in this plot: first, there is a trend with increasing L_{FIR} toward much more high-J CO luminosity compared to $J = 1-0$. This indicates a greater energy input relative to typical PDRs, to explain the high-J emission. Second, the location of the CO luminosity peak moves to higher-J with higher L_{FIR}. Third, the slope of the mid- to high-J CO emission
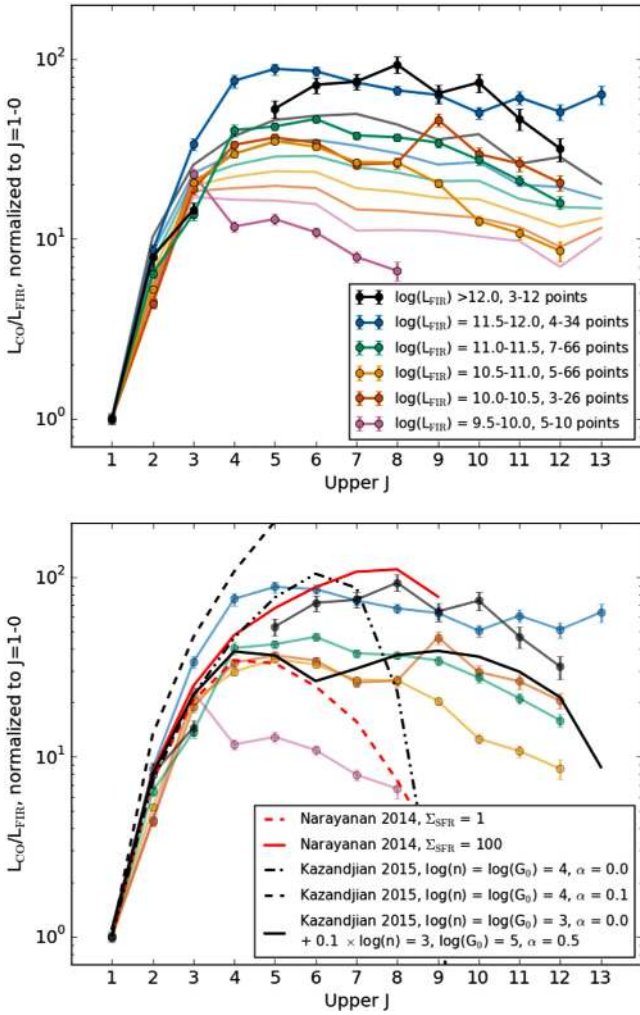
Figure 2. Top: average SLEDs by L_{FIR} ranges. For the L_{FIR} bin ranges shown in the legend, the value of L_{CO}/L_{FIR} was averaged if measurements existed for at least three galaxies. All SLEDs were then divided by the value of the L_{CO} ($J = 1-0$)/L_{FIR} line to demonstrate the difference in relative excitation (shape) of the CO ladder. The number of data points used in each SLED may change with each line, which is why a range is given in the legend. The highest luminosity bin is dominated by more distant galaxies, where the CO $J = 4-3$ line is likely to be redshifted out of the FTS band, which is why that black data point is missing. The lighter lines with no data markers indicate the predictions from the slopes in Table 4 for the center of each log bin. Bottom: comparison to theoretical models. The red model predictions are from Narayanan & Krumholz (2014) for SFR surface densities of 1 (dashed) and 100 (solid) $M_\odot$ kpc^{-2} yr^{-1} (up to $J = 9-8$). The black model predictions are from Kazandjian et al. (2015) for solar metallicity and $A_V = 10$. The first two predictions are for $n_{gas} = 10^4$, $G_0 = 10^4$, $\alpha = 0$ (dash–dot–dot, which drops quickly), and $\alpha = 0.1$ (dashed, which rises too high). The solid black line is the sum of two models, $n_{gas} = 10^3$, $G_0 = 10^3$, $\alpha = 0$ to fit the lowest-J lines, and then the model of $n_{gas} = 10^3$, $G_0 = 10^5$, $\alpha = 0.5$, multiplied by 0.1, to attempt to (although not well) reproduce a flat mid- to high-J spectrum at less than 100. The lines with data points correspond to the average SLEDs in the top panel. Note: $L_{CO} \propto \nu^3 L'_{CO}$ and $L_{CO} \propto \nu I_{CO}$ [Jy km s^{-1}].

SLED becomes flatter with increasing L_{FIR}. However, all the SLED slopes are relatively flat, none show an extreme drop-off. Fourth, the values of mid- to high-J CO relative to CO $J = 1-0$ in luminosity only range from about 10 to 100 across all lines.[13] This is consistent with the CO SLED compilation

---

[13] In brightness temperature units (L'_{CO}), this is equivalent to 0.16–1.6 for $J = 4-3$ and 0.0046–0.046 for $J = 13-12$, because $L_{CO} \propto \nu^3 L'_{CO}$.

shown in Figure 5 of K14, which showed high-J/$J = 1-0$ ratios from about 5 to 100 (with one outlier, NGC 6240, at 250 at its peak, see Meijerink et al. 2013). These last three trends are indicative of a higher *average* pressure (product of kinetic temperature and density) required to explain the shape of the CO SLED. We emphasize *average* because all of the CO emission is the sum of a gradient of conditions from different environments.

Figure 2 (top) also shows a difference between the bin-averaged SLEDs (with data points) and the SLEDs that would be predicted simply from our $\log(L_{FIR})$ versus $\log(L'_{CO})$ slopes (light colored, no data points). The predicted SLEDs span a narrower range than the bin-averaged SLEDs. Describing each CO line by a single relationship over the entire sample averages over the very real differences in populations, such as those described in Section 3.1 (e.g., different L_{CO}/L_{FIR} slopes at higher luminosities). Also, the actual weighted averages are often influenced by high S/N galaxies that may not represent the whole bin, but still illustrate the overall trend. Either way of examining the data, which we do more in the following section, shows a relatively narrow range of high-J to CO $J = 1-0$ ratios compared to expectations from some theoretical models.

4. DISCUSSION

In the previous section, we explained the observational and theoretical motivations for fitting the slopes of $\log(L_{FIR})$ versus $\log(L'_{CO})$. We now place the trends uncovered in the previous section in the context of theoretical predictions for CO emission. One may initially attempt to explain our linear slopes for the mid- to high-J CO lines using the same logic as already presented in Section 3 to describe the linear slope of the HCN $J = 1-0$ line (because the critical densities increase with upper-J level). This cannot naively be touted as the explanation for our linear slopes because the assumption of isothermality is not correct (Krumholz & Thompson 2007, Section 4.3.2). Their models rely on the gas temperature being lower than the upper-state energy level of the transition. The modeling of K14 has already shown that the kinetic temperature of the high-J emitting gas is quite high and that the lines are not thermalized; *both* temperature and density play an important role in the emission. The conditions are not uniform, and this sensitivity to both temperature and density (and invalidity of LTE) is why the high-J CO emission is not linearly related to warm molecular mass. Such a relationship (between high-J CO emission and mass) was not found in K14 for those reasons. Excitation modeling assuming statistical equilibrium parameterized by pressure (temperature $\times$ density) can better illuminate the physical conditions of the molecular gas.

Narayanan et al. (2008) extended the argument of Krumholz & Thompson (2007) by applying excitation and radiative transfer calculations to hydrodynamical simulations of disk and merger galaxies. They matched the known relations and predicted those for the (at the time) unobserved mid-J CO to be less than linear, decreasing from about 0.6 to 0.4 from $J = 4-3$ to $J = 7-6$, based on the density and temperature distributions derived from their simulations. For these lines, the decrease in the slope is due to the fraction of the emission dominated by subthermal excitation increasing with critical density of the tracer. This reiterates the above point that any one individual high-J CO line is a poor tracer of mass. We do not find such low slopes, and also do not discern any trend after
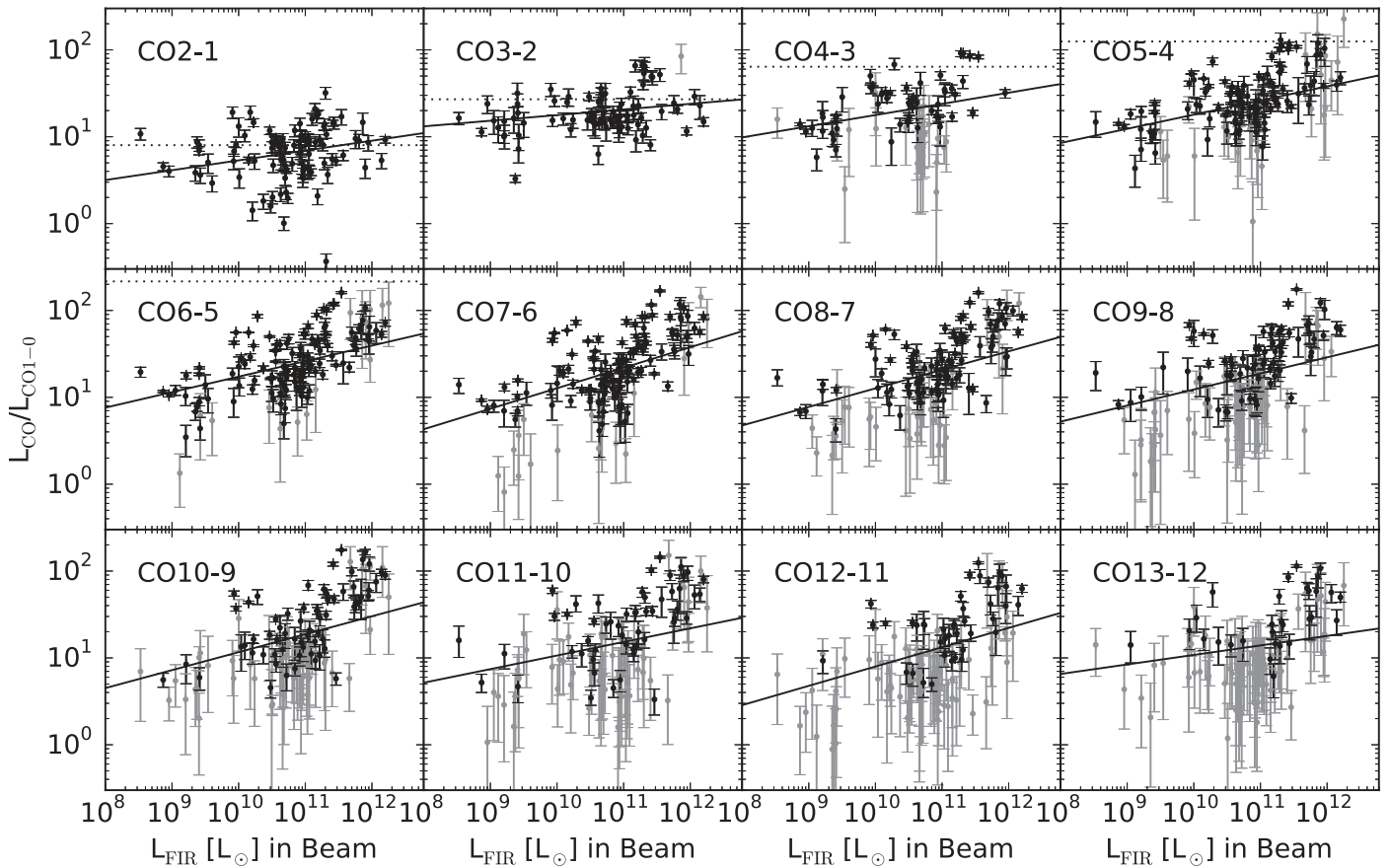
Figure 3. L_{CO}/L_{CO1-0} vs. L_{FIR}. The x-axis is the L_{FIR} in the beam for comparison to the CO measurement (see Section 2.2). The y-axis is the luminosity ratio compared to $J = 1-0$ for each line. Black data points indicate 3σ detections in both lines; gray indicate less than 3σ in the higher-J line. The dotted line denotes J_{upper}^3, the theoretical level for thermalized emission (off the top of the y-axis after $J = 6-5$). The solid line denotes the ratios based on the line fits in Table 4 (not a fit to these data, and not utilizing the same data; this plot relies on 1:1 matching of CO lines with a $J = 1-0$ measurement from the same galaxy, and multiple low-J lines from the literature are averaged together). Line ratios across the range of L_{FIR} remain generally the same across lines above $J = 6-5$, consistently between 1 or 10 to 100.

$J = 5-4$. In these relations, they strictly considered the SFR, not L_{FIR} (which we and others use as a proxy).

Narayanan & Krumholz (2014) showed that the CO SLED shape in their models can be parameterized by SFR surface density. Their simulations only considered heating by FUV photons, cosmic rays, and energy exchange with dust. FUV heating is the driving force behind PDRs. Two examples are shown in Figure 2 (bottom); some SFR surface densities are a qualitative match to our highest luminosity (and therefore highest SFR) galaxies, but only up through the mid-J lines. Although they do not predict above $J = 8-7$, the models imply a sharp drop-off would begin above this line. However, even in galaxies of two orders of magnitude lower luminosity, we still find quite flat SLED slopes in the high-J lines that are not well matched by the models, which drop off steeply after mid-J.

As already mentioned in the introduction, typical PDRs cannot account for the highly excited CO SLEDs seen in many *Herschel* spectra. The need for energy sources beyond FUV photons was demonstrated with data available from the ground (Papadopoulos et al. 2012), but *Herschel* has made it even more clear in a number of individual studies and surveys (Kamenetzky et al. 2014; Lu et al. 2014; Pereira-Santaella et al. 2014; and references within all three). Lu et al. (2014) divided the shock scenario into two categories: those associated with current SF (supernovae, winds) and those associated with other non-SF-related phenomena (AGN-driven outflows, radio jets,

or galaxy–galaxy collisions). They found that SF-dominated galaxies all had similar ratios of total mid-J ($J = 5-4$, $J = 6-5$, $J = 7-6$, $J = 8-7$, and $J = 10-9$) CO luminosity to L_{IR}, whereas galaxies with non-SF-related shocks and high AGN contribution had higher and lower ratios, respectively.

Kazandjian et al. (2015) extended the treatment of PDR models to include varying degrees of influence from mechanical heating and predicted the CO emission. They found that high-J CO line ratios are especially sensitive to mechanical heating; the same cloud conditions (parameterized as the gas density and FUV irradiating flux, n and G_0) can produce dramatically different CO SLEDs with only a few percent of the total heating contributed by mechanical energy ($\alpha = \Gamma_{mechanical}/\Gamma_{total}$) such as turbulence and winds (see their Figure 6). We examined the CO high-J/$J = 1-0$ luminosity ratios and attempted to compare the Kazandjian et al. (2015) models to our overall trends. While the addition of mechanical energy ($\alpha > 0$) can result in flatter high-J spectra, we find these ratios dramatically overpredict the high-J luminosity relative to the $J = 1-0$ line. Two examples (out of a much larger parameter space) are shown in Figure 2 (bottom) to illustrate the impact of α. With no mechanical heating, the shape of the SLED falls down too dramatically at mid-J. With the addition of mechanical heating, although the shape is flatter, it rises far above the ratios we find (and off the top of the plot), which generally do not go above 100 $L_{CO,1-0}$, and never above 180

$L_{CO,1-0}$ for 3σ detections. We can somewhat reproduce the average shape by combining multiple models with the higher excitation component reduced by a large percentage, indicating a negligible amount of CO $J = 1-0$ emission from this component. One example is shown in Figure 2, but more detailed comparisons to the models examining all the possible parameter space of the models is required.

Examination of Figure 2 indicates that our trends derived from the L_{FIR}/L'_{CO} fitting (solid, light colored lines) may not be representative of the population as a whole, given the variance in the average SLEDs from these trends. We therefore also examined the line ratios $L_{CO}/L_{CO,1-0}$ as a function of L_{FIR} in Figure 3. These data are different than those fit in Figure 1 because (a) Figure 3 relies on the high-J lines for a given spectrum having a corresponding CO $J = 1-0$ line and (b) Figure 3 averages the CO $J = 1-0$ luminosity when multiple measurements are available (although all are referenced to the same beam size). The same behavior we see in the average SLEDs is still present; the luminosity of the high-J lines relative to CO $J = 1-0$ only varies by about 1.7 orders of magnitude across the range of L_{FIR}. This is true for each of the CO lines, which is why the slopes in the average SLEDs are all relatively flat. This way of looking at the data also illustrates the differences in population, e.g., (U)LIRGs lying above the average trendline, which are averaged out when fitting the log $(L_{FIR})/\log(L'_{CO})$ slopes as in Figure 1.

We used the same method as in K14 to conduct two-component non-LTE likelihood modeling of the average CO SLEDs by the same L_{FIR} bins as in Figure 2. We describe the SLED as a sum of two components of gas, each described with four parameters: kinetic temperature, density of molecular hydrogen, column density of CO, and area filling factor. While the molecular gas exists in a continuum of conditions, two components is the simplest description of these conditions (see further discussion in K14). The product of temperature and density, the pressure P/k in K cm^{-3}, largely determines the relative shape of the SLED. The product of column density and area is proportional to the mass, which determines the total emission (and as previously discussed, in the case of the cold gas only, is often considered directly proportional to CO $J = 1-0$).

The trends with L_{FIR} for the predictions from the L_{CO}/L_{FIR} slopes (light solid colors in Figure 2) can be mostly foreseen from the shapes alone; the pressure, mass, and luminosity for both the warm and cold components increase slightly with increasing L_{FIR}, but overall the physical conditions are not too dissimilar up through $\log(L_{FIR}) = 12$. The ratio of warm to cold CO luminosity is about 45–65 for all bins $\log(L_{FIR}) < 12$, but higher for ULIRGs, around 200. The warm/cold component pressure on average drops from about 60 to 50 from the log $(L_{FIR}) = 9.5$–10 bin to the $\log(L_{FIR}) = 11.5$–12.0 bin, but is only about 25 for the highest bin of $\log(L_{FIR}) > 12$. The cold component pressures range from $\log(P/k$ [K cm^{-3}]$) = 4$ to 4.5, but 4.7 for ULIRGs, and the warm component pressures range from 5.7 to 6. Within this parameter, there is substantial degeneracy between temperature and density. Finally, the warm/cold mass ratio is about 0.2, but only 0.1 for the ULIRG bin. This means that while both the cold and warm components have higher pressure overall, more of the mid-J emission in the ULIRGs can be explained by higher bulk excitation of the total molecular gas (most of which is cold). This could have

implications for the stellar initial mass function and its subsequent effect on the surrounding gas.

In summary, we find linear slopes between mid- to high-J $\log(L'_{CO})$ and $\log(L_{FIR})$. Because this CO emission is not thermalized, it should not be used as a proxy for molecular mass or a strict K–S relation. Such slopes are inconsistent with the hydrodynamical simulations of Narayanan et al. (2008). The relative luminosity of high-J CO to $J = 1-0$ slightly correlates with L_{FIR}, but only ranges from about 10 to 100 for $J = 6-5$ through $J = 13-12$ when a single power law describes each line. When examining the full sample (Figure 3), this range varies from a few to 180. Across the range of L_{FIR} here, the SLEDs relative to CO $J = 1-0$ are fairly flat across these lines. Neither hydrodynamical nor PDR+mechanical heating models reproduce this trend when used as a single descriptor of the galaxy-wide emission. Combinations of such descriptors, which essentially adjusts the relative contributions of molecular gas components, could better describe the SLEDs.

5. CONCLUSIONS

We have presented a catalog of all CO, [C I], and [N II] lines available from extragalactic spectra from the *Herschel* SPIRE FTS.

1. Our catalog includes a uniform treatment for source/ beam coupling correction and proper estimates of the PDFs of line flux measurements given the highly correlated nature of the FTS.
2. Relations of the form $\log(L_{FIR}) = a \log(L'_{CO}) + b$ show linear slopes over multiple orders of magnitude for mid- to high-J CO lines, and slightly sublinear slopes if restricted to (U)LIRGs.
3. Average SLEDs show increasing mid- to high-J CO luminosity relative to CO $J = 1-0$, from a few to ∼100, with increasing L_{FIR}. Even for the most luminous local galaxies, the high-J to $J = 1-0$ ratios do not exceed 180.
4. The luminosities relative to CO $J = 1-0$ remain relatively flat from $J = 6-5$ through $J = 13-12$, across many orders of magnitude of L_{FIR}.
5. Current theoretical models do not reproduce such flat SLEDs with ratios < 180 across such a large range of galaxy luminosity.
6. Preliminary RADEX modeling shows that more of the mid-J emission in ULIRGs can be attributed to higher bulk excitation of the total molecular gas, not just isolated emission from high excitation gas.

Future work will include the detailed, two-component excitation modeling of galaxy spectra with at least eight of the thirteen CO lines shown here, as in K14.
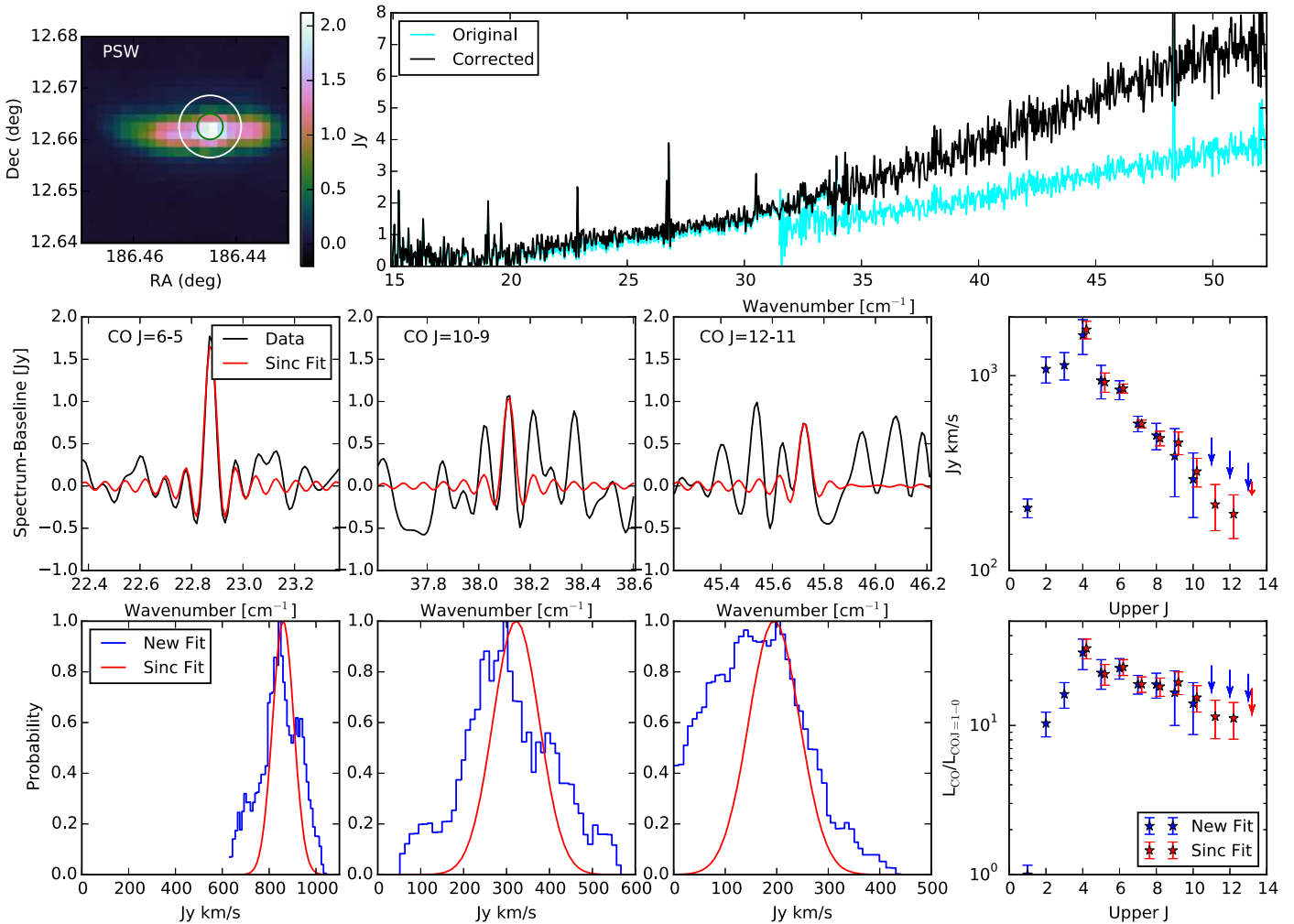
Figure 4. Line fitting of NGC 4388. Top left: the PSW map of NGC 4388 illustrates that this galaxy is extended relative to the largest and smallest spectrometer FWHM (white, green circle). As a result, the original spectrum (cyan, top right) shows a noticeable gap between the SLW and SSW bands. The source/beam size and photometer-matched corrected spectrum is shown in black (described in Section 2.2). Middle row, left three columns: zoomed-in views of the baseline-subtracted spectra (black) for three lines, and the best-fit line profile using the FTFitter (red). Bottom row, left three columns: PDFs of the integrated line fits of the row above, for the FTFitter (red, assuming a Gaussian profile and using the fit and parameter error as median and sigma), and for our new method (blue). For some lines, the distribution function is much wider, and/or more tending toward zero than the least-squares fitting routine would reveal, given the surrounding noise profile. Right column: resulting SLEDs for the line fits in Jy km s^{-1} (middle row) and in $L_{CO}/L_{CO,1-0}$ (bottom row). The original fits are shown in red; the SLED we use for fitting from our new method is in blue.

APPENDIX
ILLUSTRATED EXAMPLE OF LINE FITTING PROCEDURE

We chose NGC 4388 as an example of a semi-extended galaxy with a fairly good spectrum that degrades in S/N by the time it reaches the higher-*J* CO lines.

As an overview, the top row of Figure 4 illustrates the source/beam correction described in Section 2.2. The photometer PSW map shows that the emission is somewhat extended relative to the SPIRE FTS beam sizes, which results in a discontinuity in the original spectrum (cyan, right plot). The corrected spectrum removes this discontinuity, and shows the flux emitted in a 43″.5 beam. The bottom two rows illustrate high S/N (first column) versus poor S/N (next two columns) CO lines. Fitting these two lines with a least-squares fitting routine, such as the FTFitter, often produces integrated fluxes of S/N greater than 3, because the "ringing" in the spectrum is well-fit by the intrinsic line profile of the spectrometer. However, inspection of the lines should lead one to question why the surrounding ripple peaks are not also high detections of other lines; none of which are expected to be nearly the intensity of CO. The resulting PDFs in the bottom rows are thus wider and more heavily weighted toward zero.

To describe how the blue PDFs in the aforementioned figure were created, we focus on the CO $J = 12-11$ line, for which

the FTFitter returns an integrated flux of 0.0298 ± 0.0075 Jy cm^{-1} centered at 45.73 cm^{-1}. For this procedure, we consider the frequency range ± 2 cm^{-1} from this center, masking out $\pm$ one line profile FWHM (0.048 cm^{-1}) around any CO, [C I], and [N II] lines in this region (in this case, only the CO $J = 12$ -11 line itself). We create a grid of injected line amplitudes, f_{true} from 0 to 0.067 (the range is defined by the minimum of 0 or the flux -5σ to the flux $+5\sigma$). For each amplitude, we inject a sinc function of that amplitude at a location within our frequency range and refit the spectrum, recording the total measured integrated flux. This procedure is done at evenly sampled frequencies, every 0.048 cm^{-1}, over the frequency range (about 80 samples if no other lines are present nearby). For this input amplitude, we now have a histogram of measured amplitudes, f_{obs}. All together, we now have a two-dimensional map of input fluxes versus measured fluxes $P(f_{\mathrm{obs}}|f_{\mathrm{true}})$, from which we can back out the probability of the input flux given our measured flux. The blue PDF shown in Figure 4 is a slice of this map at measured flux of 0.0298 Jy cm^{-1} ($P(f_{\mathrm{true}}|0.0298)$; in other words, it is the distribution of input fluxes that produced a measured flux of 0.0298 Jy cm^{-1} in this frequency range.

REFERENCES

Aalto, S., Booth, R. S., Black, J. H., & Johansson, L. E. B. 1995, A&A, 300, 369
Akritas, M. G., & Bershady, M. A. 1996, ApJ, 470, 23
Alatalo, K., Blitz, L., Young, L. M., et al. 2011, ApJ, 735, 88
Albrecht, M., Krügel, E., & Chini, R. 2007, A&A, 462, 575
Baan, W. A., Henkel, C., Loenen, A. F., Baudry, A., & Wiklind, T. 2008, A&A, 477, 747
Bayet, E., Gerin, M., Phillips, T. G., & Contursi, A. 2006, A&A, 460, 467
Boselli, A., Cortese, L., & Boquien, M. 2014, A&A, 564, A65
Bothwell, M. S., Smail, I., Chapman, S. C., et al. 2013, MNRAS, 429, 3047
Carilli, C., & Walter, F. 2013, ARA&A, 51, 105
Claussen, M. J., & Sahai, R. 1992, AJ, 103, 1134
Earle, L. 2008, PhD thesis, Univ. Colorado
Eckart, A., Cameron, M., Rothermel, H., et al. 1990, ApJ, 363, 451
Elfhag, T., Booth, R. S., Hoeglund, B., Johansson, L. E. B., & Sandqvist, A. 1996, A&AS, 115, 439
Evans, A. S., Mazzarella, J. M., Surace, J. A., et al. 2005, ApJS, 159, 197
Gao, Y., & Solomon, P. M. 2004a, ApJS, 152, 63
Gao, Y., & Solomon, P. M. 2004b, ApJ, 606, 271
Garay, G., Mardones, D., & Mirabel, I. 1993, A&A, 277, 405
García-Burillo, S., Usero, A., Alonso-Herrero, A., et al. 2012, A&A, 539, A8
Greve, T. R., Leonidaki, I., Xilouris, E. M., et al. 2014, ApJ, 794, 142
Greve, T. R., Papadopoulos, P. P., Gao, Y., & Radford, S. J. E. 2009, ApJ, 692, 1432
Hailey-Dunsheath, S., Sturm, E., Fischer, J., et al. 2012, AJ, 755, 57

Harrison, A., Henkel, C., & Russell, A. 1999, MNRAS, 303, 157
Kamenetzky, J., Glenn, J., Maloney, P., et al. 2011, ApJ, 731, 83
Kamenetzky, J., Glenn, J., Maloney, P., et al. 2012, ApJ, 753, 70
Kamenetzky, J., Rangwala, N., Glenn, J., Maloney, P. R., & Conley, A. 2014, ApJ, 795, 174
Kazandjian, M. V., Meijerink, R., Pelupessy, I., Israel, F. P., & Spaans, M. 2015, A&A, 574, A127
Kennicutt, R. C. 1998, ARA&A, 36, 189
Kennicutt, R. C., & Evans, N. J. 2012, ARA&A, 50, 531
Krumholz, M. R., & Thompson, T. A. 2007, ApJ, 669, 289
Lazareff, B., Castets, A., Kim, D.-W., & Jura, M. 1989, ApJL, 336, L13
Leech, J., Isaak, K. G., Papadopoulos, P. P., Gao, Y., & Davis, G. R. 2010, MNRAS, 406, 1364
Leroy, A., Bolatto, A., Walter, F., & Blitz, L. 2006, ApJ, 643, 825
Liu, D., Gao, Y., Isaak, K., et al. 2015, arXiv:1504.05897
Lu, N., Zhao, Y., Xu, C. K., et al. 2014, ApJ, 787, 5
Maiolino, R., Ruiz, M., Rieke, G. H., & Papadopoulos, P. 1997, ApJ, 485, 552
Mao, R., Schulz, A., Henkel, C., et al. 2010, ApJ, 724, 1336
Mauersberger, R., Henkel, C., Walsh, W., & Schulz, A. 1999, A&A, 341, 256
Meijerink, R., Kristensen, L. E., Weiß, A., et al. 2013, ApJL, 762, L16
Mirabel, I. F., Booth, R. S., Johansson, L. E. B., Garay, G., & Sanders, D. B. 1990, A&A, 236, 327
Narayanan, D., Cox, T. J., Shirley, Y., et al. 2008, ApJ, 684, 996
Narayanan, D., & Krumholz, M. R. 2014, MNRAS, 442, 1411
Panuzzo, P., Rangwala, N., Rykala, A., et al. 2010, A&A, 518, L37
Papadopoulos, P. P., & Seaquist, E. R. 1998, ApJ, 492, 521
Papadopoulos, P. P., van der Werf, P. P., Xilouris, E. M., et al. 2012, MNRAS, 426, 2601
Pereira-Santaella, M., Spinoglio, L., Busquet, G., et al. 2013, ApJ, 768, 55
Pereira-Santaella, M., Spinoglio, L., van der Werf, P. P., & López, J. P. 2014, A&A, 566, A49
Pilbratt, G. L., Riedinger, J. R., Passvogel, T., et al. 2010, A&A, 518, L1
Rangwala, N., Maloney, P. R., Glenn, J., et al. 2011, ApJ, 743, 94
Rigopoulou, D., Hurley, P. D., Swinyard, B. M., et al. 2013, MNRAS, 434, 2051
Rosenberg, M. J. F., van der Werf, P. P., Aalto, S., et al. 2015, ApJ, 801, 72
Sanders, D. B., Scoville, N. Z., & Soifer, B. T. 1991, ApJ, 370, 158
Sandqvist, A. 1999, A&A, 343, 367
Sandqvist, A., Joersaeter, S., & Lindblad, P. O. 1995, A&A, 295, 585
Schirm, M. R. P., Wilson, C. D., Parkin, T. J., et al. 2014, ApJ, 781, 101
Schlingman, W. M., Shirley, Y. L., Schenk, D. E., et al. 2011, ApJS, 195, 14
Sliwa, K., Wilson, C. D., Petitpas, G. R., et al. 2012, ApJ, 753, 46
Solomon, P. M., Downes, D., & Radford, S. J. E. 1992, ApJL, 398, L29
Solomon, P. M., Downes, D., Radford, S. J. E., & Barrett, J. W. 1997, ApJ, 478, 144
Spinoglio, L., Pereira-Santaella, M., Busquet, G., et al. 2012, ApJ, 758, 108
Swinyard, B. M., Polehampton, E. T., Hopwood, R., et al. 2014, MNRAS, 440, 20
van der Werf, P. P., Isaak, K. G., Meijerink, R., et al. 2010, A&A, 518, L42
Véron-Cetty, M.-P., & Véron, P. 2006, A&A, 455, 773
Ward, J. S., Zmuidzinas, J., Harris, A. I., & Isaak, K. G. 2003, ApJ, 587, 171
Wild, W., & Eckart, A. 2000, A&A, 359, 483
Yao, L., Seaquist, E. R., Kuno, N., & Dunne, L. 2003, ApJ, 588, 771
Young, J. S., Xie, S., Tacconi, L., et al. 1995, ApJS, 98, 219
Young, L. M., Bureau, M., Davis, T. A., et al. 2011, MNRAS, 414, 940